iScience

CellPress

Article

ATF6 Is a Critical Determinant of CHOP Dynamics during the Unfolded Protein Response

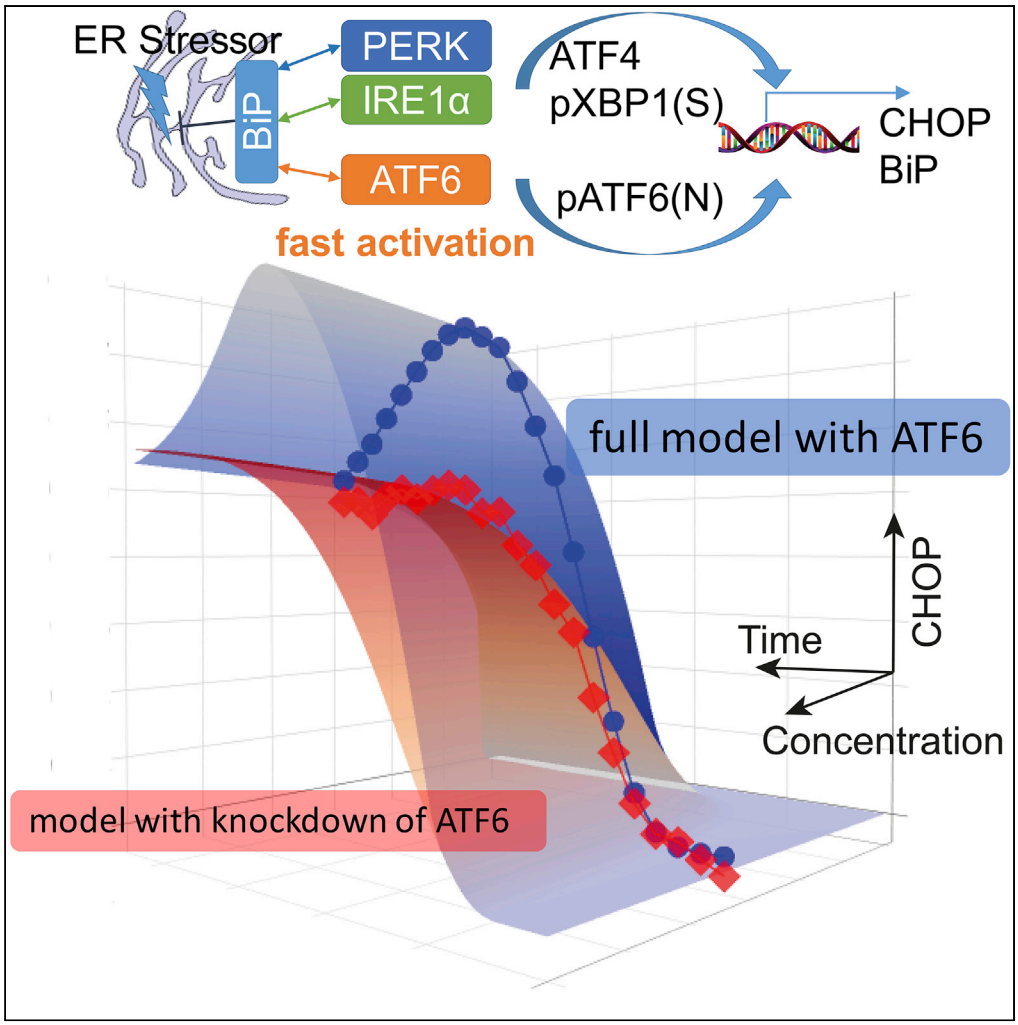

Huan Yang, Marije Niemeijer, Bob van de Water, Joost B. Beltman

water_b@lacdr.leidenuniv.nl (B.v.d.W.)
j.b.beltman@lacdr.leidenuniv.nl (J.B.B.)

HIGHLIGHTS

A mathematical model of the unfolded protein response describes microscopy data

Integration of modeling and experimental work offers insights into UPR regulation

ATF6 shapes the early dynamics of the CHOP response

Yang et al., iScience *23*, 100860
February 21, 2020
https://doi.org/10.1016/j.isci.2020.100860

iScience

CellPress

Article

ATF6 Is a Critical Determinant of CHOP Dynamics during the Unfolded Protein Response

Huan Yang,[1,3] Marije Niemeijer,[1,3] Bob van de Water,[1,2,*] and Joost B. Beltman[1,2,4,*]

SUMMARY

The unfolded protein response (UPR) pathway senses unfolded proteins and regulates proteostasis and cell fate through activity of the transcription factors ATF4, ATF6, and XBP1 within a complex network of three main branches. Here, we investigated contributions of the three branches to UPR activity in single cells using microscopy-based quantification and dynamic modeling. BAC-GFP HepG2 reporter cell lines were exposed to tunicamycin, and activation of various UPR components was monitored for 24 h. We constructed a dynamic model to describe the adaptive UPR signaling network, for which incorporation of all three branches was required to match the data. Our calibrated model suggested that ATF6 shapes the early dynamics of pro-apoptotic CHOP. We confirmed this hypothesis by measurements beyond 24 h, by perturbing single siRNA knockdowns and by ATF6 measurements. Overall, our work indicates that ATF6 is an important regulator of CHOP, which in turn regulates cell fate decisions.

INTRODUCTION

Cells activate adaptive stress responses to be able to cope with different types of stress. For instance, various chemicals cause the accumulation of unfolded proteins within the endoplasmic reticulum (ER). Drugs, such as nefazodone and diclofenac, lead to such ER stress, and as a consequence ER stress-related genes are upregulated, giving rise to the unfolded protein response (UPR), which counters chemical-induced protein stress (Ren et al., 2016; Fredriksson et al., 2014). Besides chemicals, also modifications in the rate of protein synthesis or in the cellular environment, such as nutrient level fluctuations or inflammation, can trigger the UPR (Wang and Kaufman, 2016). Moreover, the UPR can be exploited by malignant cells, assisting their development of drug resistance (Chevet et al., 2015).

Under homeostatic conditions, the ER is responsible for protein synthesis and tightly controls the correct folding and maturation of proteins by various chaperones (such as heat shock protein [Hsp] 70 and 90 family members, ER-localized DnaJ like proteins and calnexin), and foldases (such as protein disulfide isomerases and prolyl peptidylcistransisomerases). Afterward, proteins are transported to the Golgi through a secretory pathway (Braakman and Hebert, 2013). Upon disruption of ER homeostasis, cells react by activating the adaptive UPR. This will lead to an increase of the ER folding capacity, to temporary interruption of the translational machinery, and to degradation of unfolded proteins, altogether with the aim to recover from ER stress (Hetz and Papa, 2017; Wang and Kaufman, 2016).

The UPR is under control of three sensors, each activating distinct signaling cascades and transcription factors (TFs), namely, PKR-like ER kinase (PERK), inositol requiring 1α (IRE1α), and activating transcription factor 6 (ATF6) (Figure 1). These sensors are bound to the chaperone binding immunoglobulin protein (BiP/*HSPA5*) and are kept in an inactive state in unstressed conditions (Carrara et al., 2015; Shen et al., 2002). Upon ER stress, the sensors are released by BiP (Oikawa et al., 2009) or bound by misfolded proteins (Sundaram et al., 2018) enabling their activation. After activation of IRE1α in the first UPR branch, its endoribonuclease domain splices the b-ZIP TF *XBP1* mRNA resulting in the transcriptionally active protein pXBP1(S) (Calfon et al., 2002), which induces the expression of ER stress-related genes involved in protein folding (Lee et al., 2003), ER-associated degradation (ERAD) (Oda et al., 2006; Yoshida et al., 2003), and ER expansion (Shaffer et al., 2004). In the second branch, active PERK phosphorylates eukaryotic translation-initiation factor 2 (eIF2α) leading to attenuation of the translation of mRNAs, which reduces the protein load in the ER (Harding et al., 1999). Moreover, the expression of some genes, such as a b-ZIP TF ATF4, depends on the phosphorylation status of eIF2α (Lu et al., 2004). ATF4 induces the expression of ER stress-related genes to

[1]Division of Drug Discovery and Safety, Leiden Academic Centre for Drug Research, Leiden University, Einsteinweg 55, 2333 CC Leiden, The Netherlands

[2]These authors contributed equally

[3]These authors contributed equally

[4]Lead Contact

*Correspondence: water_b@lacdr.leidenuniv.nl (B.v.d.W.), j.b.beltman@lacdr.leidenuniv.nl (J.B.B.)

https://doi.org/10.1016/j.isci.2020.100860

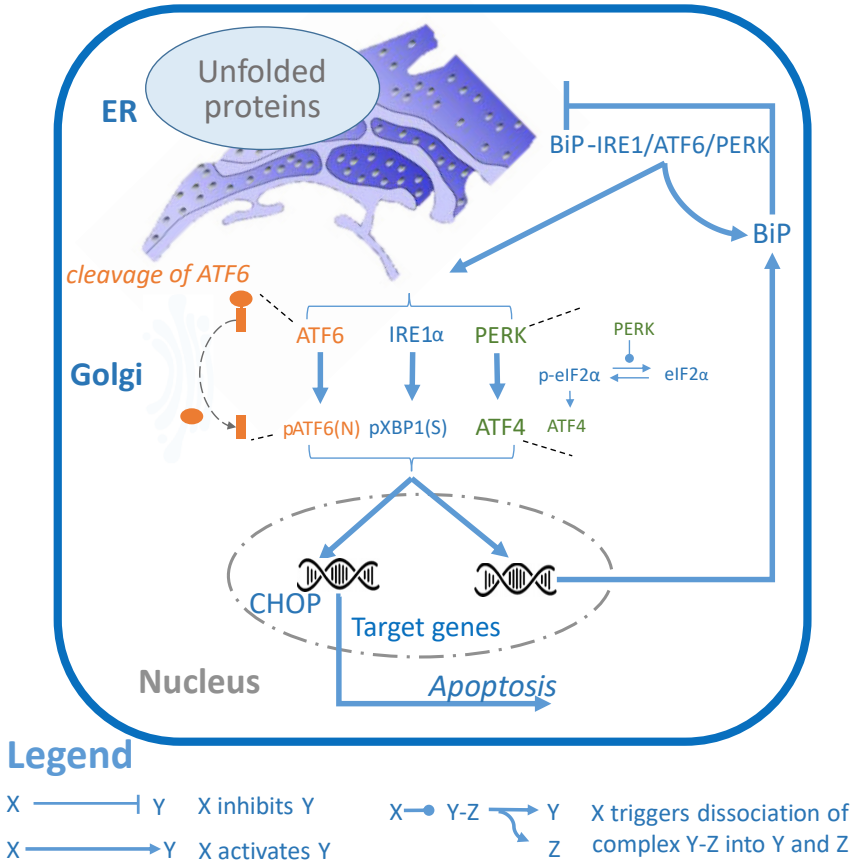

Figure 1. Cartoon Illustrating the UPR Pathway Involving Multiple Organelles and Three Branches, Several TFs, and Downstream Molecules Involved in Feedback Loops

restore homeostasis (Ameri and Harris, 2008; Han et al., 2013) and also induces the b-ZIP TF C/EBP homologous protein (CHOP), which promotes cell death (Harding et al., 2000; Urra et al., 2013; Marciniak et al., 2004). In the third branch, ATF6 translocates to the Golgi where it is cleaved (Chen et al., 2002; Ye et al., 2000). The ensuing ATF6 fragment (pATF6(N)) translocates to the nucleus and initiates the expression of its target genes such as chaperones, genes involved in ERAD, and pXBP1(S) and also of the pro-apoptotic gene CHOP (Yoshida et al., 2000, 2001; Yamamoto et al., 2007).

As many molecules have some role in the UPR network and ample feedbacks have been identified, these interactions are expected to lead to complex dynamics. To mechanistically understand these dynamics and their role in cellular adversity, mathematical modeling is an indispensable tool to quantitatively understand this complexity (Hartung et al., 2017; Kuijper et al., 2017). Ordinary differential equation (ODE) models are well fit for this purpose because they take into account laws of biochemical reactions. Several dynamical models of the UPR have already been built by various groups. Cho et al. (2013) utilized discrete dynamical modeling to study a complex UPR network model, considering different biological processes to occur at similar time scales. With respect to ODE models applied to the UPR, several studies focused on details of UPR sub-modules, e.g., on the IRE1α branch (Pincus et al., 2010). Taking into account all three branches, Erguler et al. (2013) proposed a comprehensive UPR model and highlighted potential emerging dynamics due to feedback loops. A simpler three-branch model was derived using steady-state assumptions by Trusina et al. (2008), which was subsequently used to study repeated exposure and the effect of different types of stress during *in silico* simulations (Trusina and Tang, 2010). Interestingly, this work emphasized the potential importance of BiP accumulation during primary exposure leading to protection against renewed ER stress. Recently, Diedrichs et al. (2018) integrated gene expression data from mouse embryonic fibroblasts into a UPR model and validated their model predictions with knockout experiments, which focused on the

feedback loop via CHOP-induced DNA damage-inducible protein 34 (GADD34) that leads to dephosphorylation of eIF2α and a consequent increase in protein load.

To further increase our mechanistic understanding of regulation of UPR TF activity during adaptation, we here present a new ODE model that we calibrate with a rich set of dynamic high-content imaging data. These data are generated utilizing our established liver carcinoma HepG2 BAC-GFP reporter platform (Wink et al., 2017, 2018; Poser et al., 2008). The usefulness of combining high-content imaging of HepG2 reporter cell lines with mathematical modeling has recently been demonstrated for the NFκB-mediated inflammatory stress pathway (Oppelt et al., 2018). Here, by applying high-content confocal imaging to HepG2 BAC-GFP UPR reporters for CHOP, ATF4, pXBP1(S), and BiP, we were able to precisely follow the activation dynamics of these UPR genes in response to a broad concentration range of tunicamycin, a highly specific ER stress inducer. By fitting our dynamic model to the data, we dissected the contribution from single branches to UPR regulation. Furthermore, model selection suggested that ATF6 has an important role in shaping the CHOP dynamics during ER stress. Consistent with this, siRNA-mediated silencing of ATF6 led to diminished CHOP induction during the acute phase, yet resulted in a prolonged induction of CHOP. This suggests that ATF6 is an important regulator for cell fate decisions under chronic ER stress.

RESULTS

Image-Based Monitoring of UPR and Cellular Dynamics

To establish an ODE model that captures UPR network regulation and activation, experimental data are required that quantify the dynamics of induction of crucial UPR genes with a dense time resolution. We achieved such a resolution by combining our previously established liver carcinoma HepG2 BAC-GFP UPR reporters (Wink et al., 2017, 2018) with high-content confocal microscopy. We used the compound tunicamycin as an ER stress inducer, which inhibits N-glycosylation and therefore leads to the accumulation of unfolded glycoproteins (Yoo et al., 2018). Tunicamycin specifically induces ER stress and is therefore an excellent compound to create a UPR-specific ODE model.

We first examined whether our HepG2 UPR reporters for CHOP, ATF4, pXBP1(S), and BiP are representative for the behavior of wild-type (WT) HepG2 cells. To this purpose, we established the protein expression of endogenous CHOP, ATF4, pXBP1(S), and BiP using western blotting in HepG2 WT cells after tunicamycin exposure for 4, 8, 16, and 24 h. Both treatment with 1 and 6 μM tunicamycin resulted in a clear induction of UPR proteins (Figure 2A). However, BiP was already highly expressed at basal levels and therefore it was unclear whether further induction occurred. A high tunicamycin concentration of 6 μM led to an earlier induction of UPR proteins than a low concentration of 1 μM (Figure 2A).

Next, we assessed if all four HepG2 UPR reporters behaved similarly upon tunicamycin exposure as WT cells. Applying a TempO-seq targeted transcriptomics approach to all five HepG2 (WT and reporter) cell lines exposed to a broad concentration range of tunicamycin for 8 or 24 h revealed that *DDIT3* (i.e., the gene coding for the CHOP protein) expression across HepG2 wild-type and BAC-GFP cell lines followed a similar dose response at both time points (Figure 2B). For other UPR-related genes, the different cell lines also have a similar dose response behavior and are highly correlated in gene expression (Figure S1). As expected based on having at least one additional copy of the gene, HepG2 CHOP-GFP exhibited a slightly higher *DDIT3* expression at baseline compared with the other lines, but this did not influence the dose response of *DDIT3* itself (Figure 2B) or the expression of other UPR-related genes (Figure S1). Thus, all HepG2 UPR reporter behave similarly with respect to UPR gene expression.

To generate dynamic protein expression data to which results from an ODE model can be compared, we exposed HepG2 BAC-GFP UPR reporters for CHOP, ATF4, pXBP1(S), and BiP to a concentration range from 1 to 100 μM of tunicamycin and subsequently applied live imaging with confocal microscopy to capture the GFP induction in single cells and total cell count every hour until 24 h of exposure (Figures 2C and 2D). The dynamic pattern of CHOP-GFP expression exhibited a peak around 10–20 h (Figures 2C and 2D), which was consistent with the CHOP expression in WT HepG2 cells observed with western blotting (Figure 2A). Increasing concentrations of tunicamycin led to earlier maxima of CHOP expression levels (Figure 2C). For all four reporters, a concentration-dependent increase in maximal GFP intensity occurred. However, at the highest concentration (100 μM) of tunicamycin, the maximal GFP intensity was equal or lower compared with that of 50 μM, which is indicative of cellular toxicity. Consistent with this interpretation, the total number of cells dramatically decreased at 100 μM of tunicamycin (Figure 2E). At 50 μM of

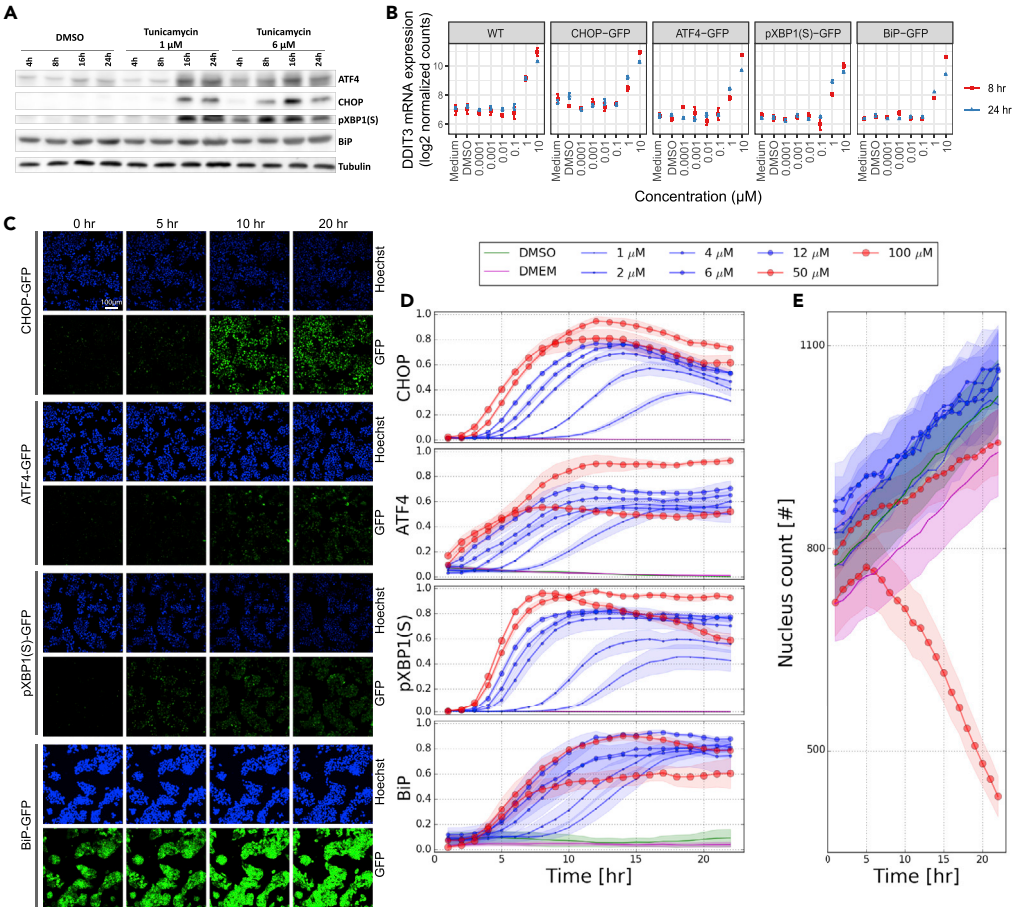

Figure 2. Dynamic Measurements of Various UPR Components to Integrate with Modeling

(A) Western blot of CHOP, ATF4, pXBP1(S), and BiP protein at 4, 8, 16, and 24 h upon exposure to DMSO or tunicamycin (1 and 6 μM) in WT HepG2 cells. Tubulin was used as protein loading control.

(B) Log2 normalized counts of DDIT3 mRNA expression analyzed using TempO-seq transcriptomics at 8 or 24 h after exposure with various concentrations of tunicamycin in HepG2 WT and UPR BAC-GFP reporter cell lines.

(C) Representative images of HepG2 UPR BAC-GFP reporter cell lines (CHOP, ATF4, pXBP1(S), and BiP) stained with Hoechst for nuclei visualization. Images were obtained using confocal microscopy with a 20× objective at the indicated time points after exposure to tunicamycin at 6 μM. Hoechst is represented in blue (upper rows) and GFP in green (lower rows).

(D and E) Quantification of single-cell-based GFP intensity of the HepG2 UPR BAC-GFP reporter cell lines after min-max normalization (D) and cell counts (E) after exposure to DMEM/DMSO or to a broad concentration range of tunicamycin and imaged live every hour for 24 h after exposure using confocal microscopy. BiP-GFP intensity was quantified in the cytoplasm; all other reporters were quantified in the nuclei.

Data in (B), (D), and (E) represent mean and standard error of the mean (SE) of three biological replicates.

tunicamycin, there was also a slower increase in cell count over time compared with lower concentrations. Therefore, only concentrations below 50 μM of tunicamycin were taken along for the ODE-model development since we here focus on the adaptive UPR signaling network. In summary, the gene expression as well as protein expression levels of BAC-GFP HepG2 UPR reporter cell lines and WT HepG2 cells exhibited similar baseline levels and dynamic patterns upon exposure to tunicamycin. Therefore, we concluded that the BAC-GFP UPR cell lines were sufficiently representative for WT HepG2 cells to be used for subsequent dynamical modeling.

UPR Model with ATF6 Provides Excellent Fit to the Data

Because we had dynamic information on four BAC-GFP reporter cell lines, we initially constructed an ODE model with four variables representing the protein expression level for these reporters as well as a variable

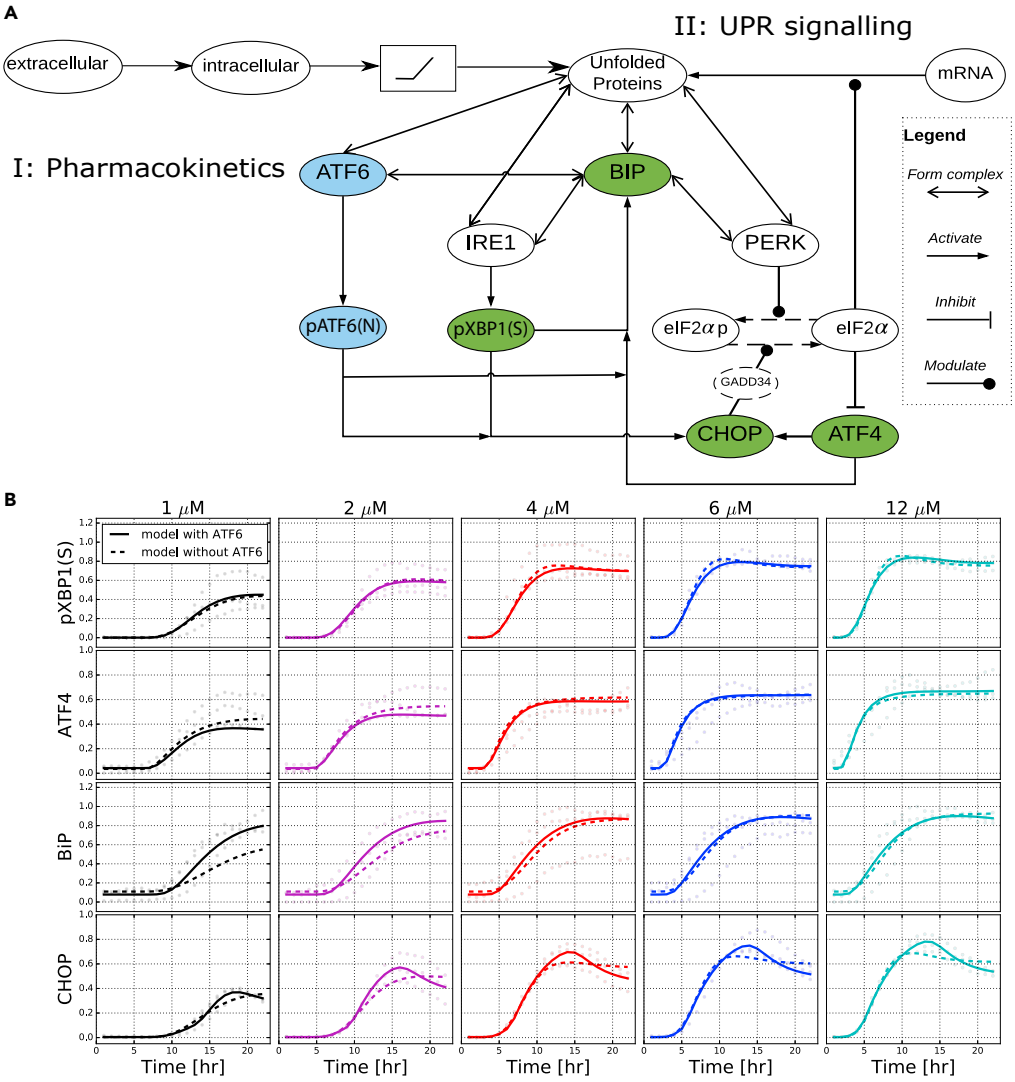

Figure 3. Model Structure and Fit

(A) Schematic diagram of the modeled UPR pathway with both pharmacokinetics and signaling network.

(B) Model fits to the experimentally observed levels of pXBP1(S), ATF4, BiP, and CHOP upon tunicamycin exposure at five concentrations. Dots present values for three replicates. Optimized fits from models with ATF6 branch (solid curves) or without (dashed curves) are plotted.

for the amount of unfolded proteins in the cell (Figure 3A). This model was a modification of an earlier published model by Trusina et al. (2008). We did not incorporate ATF6 explicitly, but it was considered to behave similarly to IRE1α, i.e., these sensors were considered to be in quasi steady state (Trusina et al., 2008). In addition, we modeled the downstream molecules ATF4 and CHOP. Finally, because the experimentally observed dynamics of intensity of all UPR reporters exhibited a concentration-dependent delay of activation for tunicamycin concentrations below 12 μM (Figure 2D), we incorporated this phenomenon in a pharmacokinetic module preceding the signaling module. Specifically, we added a threshold in the effective intra-cellular concentration of tunicamycin, i.e., we consider the UPR signaling to be triggered only when a particular intra-cellular stress level is crossed, which leads to some delay of pathway activation (see simulated pharmacokinetic profiles in Figure S2).

This initial model could roughly describe the reporter dynamics, yet this could not capture the consistently observed dynamic peak in CHOP expression (Figure 3B, dashed line). Therefore, we also created a model variant including the ATF6 branch explicitly (for which no BAC-GFP reporter cell line was available). The

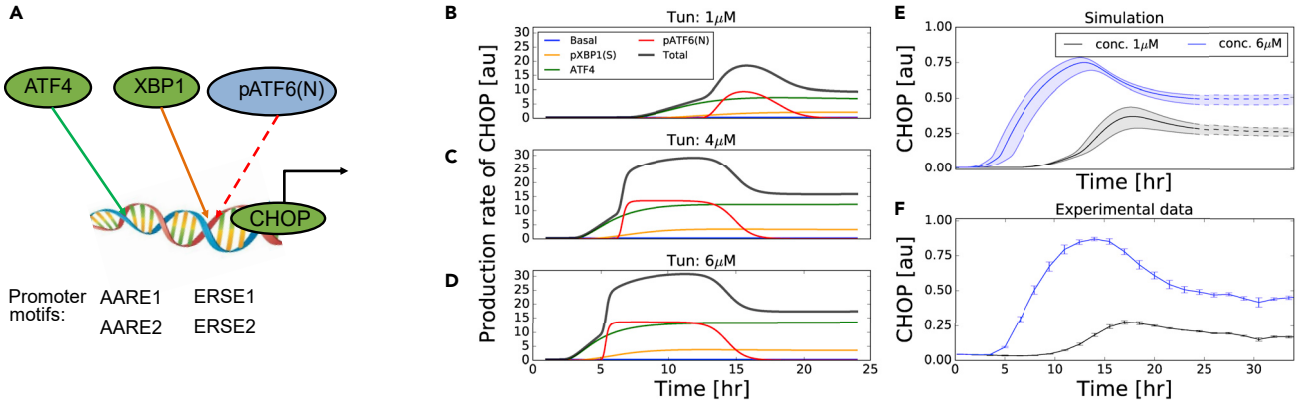

Figure 4. Model-Based Prediction of CHOP Transcription

(A) Illustration of the TFs contributing to CHOP transcription.

(B–D) Simulations of the contributions of pXBP1(S), ATF4, and pATF6(N) to the CHOP production rate after exposure to tunicamycin concentrations of 1 (B), 4 (C) and 6μM (D), respectively.

(E) Model prediction of CHOP levels within the first 24 h (solid line) and between 24 and 34 h (dashed line). Simulations were conducted with various strengths of exposure (between 30% and 130% of the reference value) shown as shaded areas.

(F) Image-based experimental observation of CHOP for 34 h represented as the mean ± SE of three biological replicates.

model with all three UPR branches contains 47 parameters, whereas the model without ATF6 has 39 parameters (for equations see Transparent Methods). After fitting of both models to the experimental data (for parameter estimates see Table S1, for their estimated standard errors see Figure S3, and for their sensitivity see Figure S4), visual comparison of the two model variants showed that only the model with ATF6 was able to describe the CHOP peak (Figure 3B, solid line). This visual impression was confirmed by application of a likelihood-ratio-based approach to compare the models with the data (ΔG = 119 and 271 for the full and ATF6-free models, respectively; $p < 0.001$), and by calculation of the information criteria AIC and BIC (Pawitan, 2001) for the two competitive models (AIC full model: 2×119 + 2×47 = 332; AIC ATF6-free model: 2×271 + 2×39 = 620; BIC full model: 2×119 + ln(440) 47 = 524.08; BIC ATF6-free model: 2×271 + ln(440) 39 = 779.38). The above results thus suggest that the ATF6 branch plays an important role in shaping the early CHOP dynamics, and we continued with the calibrated model including ATF6 for further exploration and validation.

Model Correctly Predicts CHOP Dynamics beyond 24 Hours

The transcription of CHOP can be induced by binding of UPR TFs, i.e., ATF4, pXBP1(S), and pATF6(N), at the AARE and ERSE promoter motifs (Figure 4A [Takayanagi et al., 2013; Oyadomari and Mori, 2004]). However, previous work has suggested that induction of CHOP is predominantly regulated by ATF4 and pATF6(N), and to a minimal extent by pXBP1(S) (Diedrichs et al., 2018; Wu et al., 2007; Ma et al., 2002). Having the parameterized full UPR model in place allowed us to explore both the speed of activation of the three sensors and the contribution of each of the three downstream TFs to CHOP induction at different time points. With respect to the speed of activation of the sensors, ATF6 is the sensor responding most quickly, followed by IRE1α and finally PERK (Figure S5). With respect to the contribution of the downstream TFs to CHOP transcription, we investigated this by separating the mathematical term representing the CHOP production rate into the individual TF contributions forming this term. This analysis showed that the ATF6 branch shapes the early dynamics of CHOP production, whereas ATF4 dominates the CHOP production at late time points (Figures 4B–4D). This explains why ATF4 is typically considered the primary TF responsible for CHOP production (Scheuner et al., 2001; Harding et al., 2000), yet our analysis suggests that pATF6(N) also has an important contribution to CHOP production at early time points. This happens because pATF6(N)-mediated CHOP transcription starts and ends relatively abruptly owing to the high cooperativity (n = 46.32 in the best fit) in the Hill function describing pATF6(N) activity. Once pATF6(N) drops below the Hill threshold K_{A2C} (which equals 0.717 in the best fit), the effect of the still relatively high pATF6(N) levels on CHOP transcription quickly becomes negligible. Note that such a high cooperativity is required to explain the exact height of the CHOP peak (Figures S6–S8). Furthermore, our analysis confirmed the minimal role of pXBP1(S) in CHOP transcription, which is due to low pXBP1(s) levels rather than to low TF activity of the present pXBP1(s) (Figure S9).

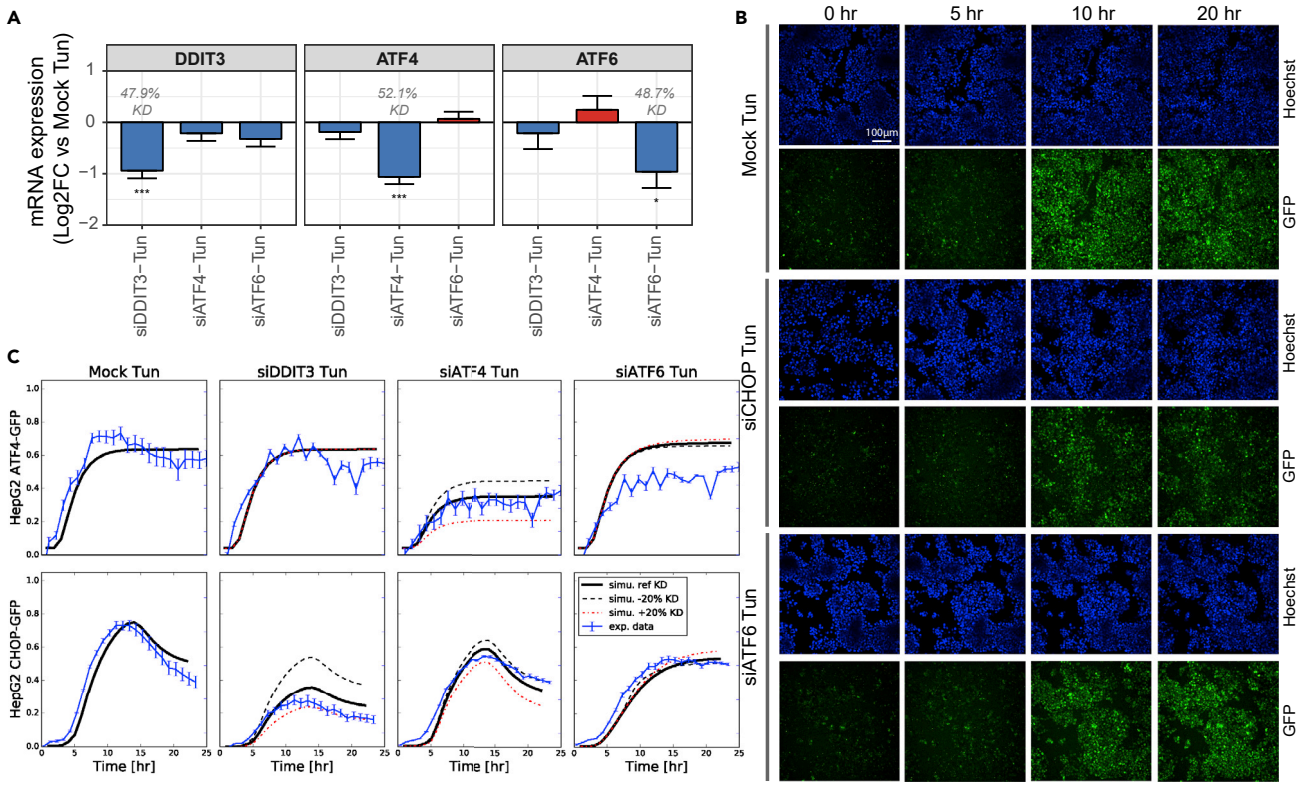

Figure 5. Perturbation of UPR with siRNA Knockdowns Are Consistent with Model Predictions

(A) Log2 fold changes of mRNA expression of different siRNA-mediated gene knockdowns relative to siRNA mock negative control in HepG2 WT cells exposed to 6 μM of tunicamycin for 16 h, determined using TempO-seq transcriptomics. Knockdown efficiencies of siRNAs are depicted in gray numbers. Data represent the mean ± SE of three biological replicates.

(B) Representative confocal microscopy images obtained with 20× objective of HepG2 CHOP-GFP reporter cells exposed to 6 μM of tunicamycin for 16 h after CHOP, ATF6, or Mock siRNA. To visualize the nuclei, cells were stained with Hoechst (upper rows), and CHOP-GFP is represented in green (lower rows).

(C) Model simulation of ATF4 and CHOP (black curves) compared with quantified GFP data after exposure to 6 μM of tunicamycin for different siRNA-mediated knockdown conditions (blue line and error bars representing mean ± SE of three biological replicates). Simulations with varied knockdown efficiency (black dashed: 20% less, red dashed: 20% more) are also plotted.

Given the model prediction that the ATF4-driven CHOP production rate remains relatively high around 24 h, we simulated the model for a duration longer than the 24 h on which the parameterization was based. Beyond 24 h the CHOP level was predicted to stay around the same level for tunicamycin concentrations of 1 and 6 μM (Figure 4E) rather than quickly returning to baseline level. Our simulations predicted that this was due to a gradual increase of the intra-cellular stress levels, which saturated after ~20 h and did not yet decrease (Figure S2). The sustained high ATF4 level is attributed to its upstream molecules PERK and eIF2α that tightly follow the dynamics of the intra-cellular stressor and of unfolded protein (Figure S9). To validate this model prediction, we performed imaging experiments of a duration beyond 24 h, which showed that indeed CHOP-GFP levels in HepG2 cells remained at a relatively high level up to 34 h (Figure 4F). Thus, although the model was based on 24-h measurements, it correctly predicted sustained CHOP levels beyond 24 h.

Knockdown Experiments Confirm Role of ATF6 in CHOP Dynamics

We next challenged our model further by evaluating the effect of perturbing single UPR-related genes, including ATF6, on activation of other UPR components using siRNA-mediated silencing. To confirm success of knockdown by siRNA and to quantify its efficiency, we first measured the expression of *DDIT3*, *ATF4*, and *ATF6* after knockdown of these separate genes for 3 days and subsequent exposure to 6 μM tunicamycin for 16 h. TempO-seq transcriptomics experiments showed that expression of these genes was indeed significantly decreased by siRNA-mediated silencing upon exposure to tunicamycin (Figure 5A). To study the effect of perturbation of UPR-related genes on CHOP and ATF4 induction dynamics during

ER stress, we then measured CHOP-GFP and ATF4-GFP in HepG2 BAC reporters using confocal imaging for 24 h after 6 μM tunicamycin exposure when no gene (Mock), *DDIT3*, *ATF4*, or *ATF6* was silenced using siRNA (Figure 5B and blue lines in Figure 5C). Knockdown of *DDIT3* and *ATF4* led to reduced levels of, respectively, CHOP-GFP and ATF4-GFP, confirming the success of the knockdowns also at protein level. We then compared the experimental measurements upon knockdown with model predictions incorporating the knockdown efficiencies that we measured for the different genes (Figure 5C).

ATF4 and *ATF6* knockdown both affected the CHOP-GFP dynamics, yet its effect was qualitatively different. *ATF4* knockdown led to a decrease in CHOP induction, yet a clear peak remained present in the CHOP dynamics around 16 h post tunicamycin exposure, indicating that ATF4 is not responsible for that peak (Figure 5C). Similarly, *ATF6* knockdown led to a reduced CHOP induction specifically in the initial phase. However, after 16 h of exposure, CHOP levels did not decline again and CHOP levels at 24 h were slightly higher when ATF6 was silenced than for the Mock control. Our model offers an explanation for these observations: First, the lowered activity of pATF6(N) due to ATF6 knockdown implies that the CHOP transcription rate contributed by pATF6(N) does not exceed the required threshold and that CHOP transcription fully depends on XBP1(S) and ATF4 activity. Second, the reduced pATF6(N) upon knockdown also lowers BiP expression, thus leading to an increased amount of unfolded proteins, XBP1(S) and ATF4, which in turn slightly increases CHOP expression around 24 h compared with a setting without knockdown (Figure S10). Thus, ATF6 affects the CHOP dynamics especially in the initial phase and also slightly in the later phase as was predicted by our model. Altogether, the experimentally observed alterations in ATF4 and CHOP induction could be accurately predicted with our model and this analysis confirmed the model prediction that ATF6 shapes CHOP dynamics. As ATF6 shapes the dynamic pattern of pro-apoptotic CHOP, i.e., initially increases CHOP but later decreases it owing to initial BiP-mediated folding of unfolded proteins, we speculate that early ATF6 activity may in fact protect cells under chronic ER stress. This is consistent with experimental findings in ATF6 knockout mice in which cell death increased upon exposure to tunicamycin after 18 h (Wu et al., 2007).

ATF6 Activation Peaks Early as Predicted by Modeling

Since our model predicts that the peak in CHOP dynamics that follows tunicamycin exposure is due to early ATF6 activity, we evaluated the mRNA expression and activation dynamics of endogenous ATF6 in HepG2 WT cells by TempO-seq transcriptomics and western blot. ATF6 mRNA expression increased by 2-fold at 10 μM of tunicamycin at 8 and 24 h, but not at 1 μM (Figure 6A), suggesting minor upregulation of ATF6 only at high concentrations. At protein level, exposure to 6 μM of tunicamycin clearly led to the expected inhibition of N-glycosylation, which became visible by the appearance of a low western blot band representing unglycosylated, uncleaved ATF6 ($ATF6_{UG}$) and a decrease of the high band representing glycosylated ATF6 ($ATF6_{G}$) starting from 4 h of exposure (Figure 6B; quantification in Figure 6C, first two panels). Exposure to a lower concentration of 1 μM tunicamycin also increased the formation of $ATF6_{UG}$, yet it was only apparent at late time points (Figure S11).

The relation between $ATF6_{G}$ and $ATF6_{UG}$, which changes during tunicamycin exposure, is illustrated in Figure 6D, i.e., both forms can degrade, but only $ATF6_{G}$ can lead to pATF6(N). The amount of total uncleaved ATF6 (i.e., $ATF6_{UG}$ + $ATF6_{G}$) decreased at early time points (6 h, $p = 0.016$; 8 h, $p = 0.070$) compared with DMSO control but restored later on (Figure 6C third panel). Since levels of endogenous cleaved ATF6 in HepG2 cells were difficult to capture using western blot, we assessed ATF6 cleavage from the difference in total uncleaved ATF6 levels. Considering the ATF6 production and degradation rates to remain roughly unchanged at early time points in tunicamycin and DMSO conditions, the decreased amount of total uncleaved ATF6 at those time points can be attributed to ATF6 cleavage. Therefore, we used the difference in total uncleaved ATF6 between the first measured time point and subsequent time points as a measure for ATF6 cleavage (Figure 6C, panel 4). The level of pATF6(N), as estimated through this approach, peaked at 6 h post tunicamycin exposure ($p = 0.044$), which is consistent with the dynamics of predicted free ATF6 and pATF6(N) in our computational model (Figure 6E).

In conclusion, the activation dynamics of ATF6 were early and concentration dependent as predicted by our model. Together, our combination of experimental and computational modeling work shows that ATF6 is activated early after tunicamycin exposure and that this causes an early rise in CHOP expression. The CHOP expression subsequently drops to a lower level yet remains relatively high owing to ongoing presence of stress, keeping ATF4 expression at elevated levels.

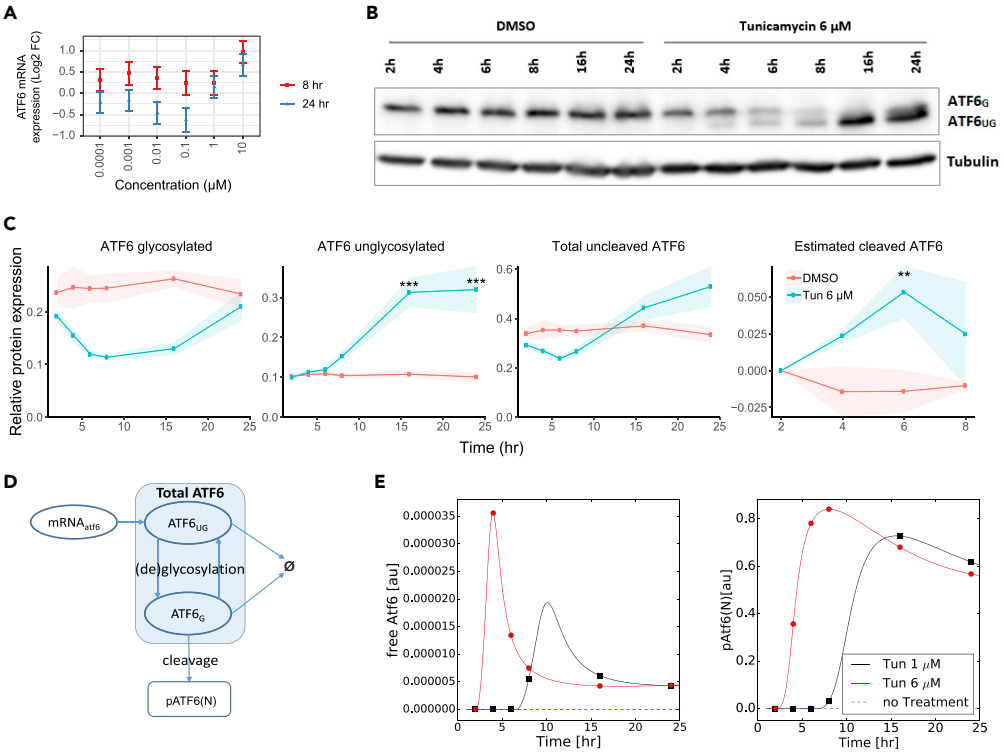

Figure 6. Matching ATF6 Dynamics in Experiment and Model

(A) ATF6 mRNA expression after 8 or 24 h of exposure to a broad concentration range of tunicamycin in HepG2 WT cells using TempO-seq, represented as the mean of log2FC ± SE of three biological replicates.

(B) Western blot of uncleaved ATF6 (G, glycosylated, UG, unglycosylated) measured in HepG2 WT cells at 2, 4, 6, 8, 16, or 24 h after exposure to tunicamycin (6 μM) or DMSO. As protein loading control, tubulin protein expression was assessed.

(C) Quantified protein expression of the indicated ATF6 forms from three biological replicates after protein loading correction using tubulin (symbols and shaded area represents mean ± SE with the significance levels represented as $^{**}p_{adj} < 0.05$, $^{***}p_{adj} < 0.01$). Cleaved ATF6 was estimated based on the difference between total uncleaved ATF6 at 4, 6, and 8 h versus the 2-h time point.

(D) Diagram of relation between different ATF6 forms during tunicamycin treatment, where $ATF6_G$ and $ATF6_{UG}$ represent glycosylated and unglycosylated forms, respectively.

(E) Model-predicted dynamics of free ATF6 and the downstream pATF6(N) upon exposure of tunicamycin at 1 and 6 μM.

DISCUSSION

The basis of our work consisted of dynamic measurements detailing the induction of UPR regulators in HepG2 reporter cell lines during tunicamycin-induced ER stress. We exploited these data to establish a computational model representing the essential mechanisms shaping the UPR and fitted the model using 24-h reporter dynamics. The strength of our approach was that we exploited a large amount of high-content imaging data to obtain a quantitative understanding of UPR regulation. This combination of modeling and experiments helped to unravel the role of different molecules in the UPR dynamics. Specifically, the model predicted that the ATF6 branch was required to explain the observed UPR dynamics and this prediction was verified by knockdown experiments, prolonged experimental time courses, and additional western blot measurements.

Some of the previously published UPR modeling work focused on theoretical understanding of network dynamics in different scenarios (Trusina et al., 2008; Erguler et al., 2013). Specifically, in the extensive model of Erguler et al. (2013), it was shown that the network could exhibit different kinds of structural behavior depending on the parameter settings. For example, for some parameter conditions oscillations occur, showing that the network is in principle capable of generating such behavior. However, our combined modeling and experimental analysis demonstrates that at least for HepG2 cells exposed to tunicamycin such oscillations do not occur. Owing to the complexity of the model by Erguler et al. (2013) precluding

calibration to a dataset that was limited in terms of number of monitored variables, we instead chose to extend the model by Trusina et al. (2008) with CHOP and ATF6, rendering a new model with similar UPR TF activity that could be calibrated to our imaging data. A combination of experimental and computational work similar to ours has been recently reported by Diedrichs et al. (2018), where model predictions were based on qPCR and western blot experiments. Key differences with our approach include the choice of test compound and the balance of model complexity and measurements. With respect to the employed compounds, Diedrichs et al. (2018) exposed MEFs to thapsigargin, a SERCA inhibitor disturbing calcium homeostasis, whereas we used tunicamycin, which inhibits N-glycosylation within the ER. The downside of using exposure to thapsigargin is that it not only leads to a strong UPR induction but also induces oxidative stress, at least in HepG2 cells (Wink et al., 2017). With respect to model complexity and the amount of experimental data, time-lapse imaging data has a major advantage that it easily delivers many data points at the single-cell level within specific sub-cellular compartments, i.e., we have more than 400 datapoints measured from four BAC-GFP reporters at five concentrations and at more than 20 time points.

Besides capturing the dynamics of UPR-related molecules, our quantitative modeling approach suggests that ATF6 is responsible for the early peak of CHOP. Both our knockdown experiments and ATF6 measurements using western blotting at different time points are consistent with this hypothesis. Specifically, the decrease in total uncleaved ATF6 strongly suggested that cleavage of ATF6 peaked at early time points (around 6 h). These findings are also consistent with those of Yoshida et al. (2001), who reported a similar pattern with an overshoot in the nuclear active ATF6 fragment after tunicamycin treatment in HeLa cells. To verify the observed activation dynamics of ATF6 and to capture high-resolution activation dynamics at sub-cellular localization, future imaging-based dynamic readout of ATF6 and its fragments would be highly valuable. Based on such data, the part of our model describing ATF6 could also be extended and better parameterized.

The parameters in our mechanistic model have a biological interpretation, and their estimates thus provide quantitative insight into UPR regulation. First, the degradation rate of the protein CHOP (r_C) was estimated to be 5-fold larger than that of BiP (r_B), i.e., a similar difference as found by Rutkowski et al. (2006). Given the protective role of BiP through protein folding and the pro-apoptotic role of CHOP, this suggests that the distinct degradation rates represents one mechanism that explains initial adaptation to ER stress, followed by a switch toward adversity during prolonged ER stress. Second, the parameters K_{BP}, K_{BI}, and K_{BA} shape the response sensitivity among the three UPR branches PERK, IRE1α, and ATF6, with the latter being the quickest (Figure S5). Interestingly, we showed that ATF6(N) transcriptional activity with respect to CHOP is also switched off early and abruptly owing to the high predicted cooperativity of this response (Figure 4).

In response to ER stress, cells have several coping strategies to eliminate the accumulation of misfolded proteins by activating the three UPR branches. However, in case ER stress becomes too severe or chronic, apoptotic signaling pathways will be activated and cells will switch from adaptive to pro-apoptotic signaling. In this switch, CHOP plays an important role through various mechanisms (Urra et al., 2013; Uzi et al., 2013; Ji et al., 2005) and therefore regulators of CHOP can affect the sensitivity of cells to ER stress. Here, we found that ATF6 has such a crucial role in the dynamics of CHOP induction, where perturbation of ATF6 led to absence of the initial CHOP peak yet led to slightly increased CHOP levels at a later stage. Our findings are consistent with earlier work in which ATF6-knockout MEFs had lower CHOP levels until 12 h of exposure to thapsigargin, whereas at later time points CHOP levels were higher compared with WT (Diedrichs et al., 2018). Given the importance of ATF6 in the regulation of CHOP activation dynamics as well as cytoprotective proteins such as BiP (Vitale et al., 2019), ATF6 is also expected to play a role in the switch between adaptive to cellular adversity, especially in realistic scenarios with repeated exposure to chemicals. Indeed, it has been reported that ATF6 plays a role in the protection against chronic ER stress using ATF6 knockout mice and repeated exposures (Wu et al., 2007).

In conclusion, by combining high-throughput confocal imaging and ODE modeling, we captured the dynamics and role of individual components within the UPR, particularly pinpointing the importance of ATF6 in CHOP activation dynamics. Since the UPR plays an important role in both drug-induced toxicity as well as the development of drug resistance in cancer, improved insight in UPR signaling dynamics in relation to cell fate is important.

Limitations of the Study

Using a combined experimental and computational modeling study of UPR signaling, we showed that ATF6 has an important role in shaping the dynamic pattern of CHOP activity, thus likely affecting cell

fate decisions under ER stress. However, we neither mathematically described the relation between UPR activity and cell fate, nor did we investigate experimentally whether cell fate decisions are indeed affected by ATF6. Moreover, our findings are based on a single cell line and only on *in vitro* observations, hence the response may be different in *in vivo* scenarios. Finally, we do not know whether our observations hold for other UPR-invoking compounds and whether our model is able to describe UPR dynamics for such compounds, including their potential adversity.

METHODS

All methods can be found in the accompanying Transparent Methods supplemental file.

DATA AND CODE AVAILABILITY

We put the python script to simulate the developed computational model as the Supplemental Information.

SUPPLEMENTAL INFORMATION

Supplemental Information can be found online at https://doi.org/10.1016/j.isci.2020.100860.

ACKNOWLEDGMENTS

This work has received funding from the ZonMW InnoSysTox program under grant agreement No 40-42600-98-14016 (to J.B.B. and B.v.d.W.) and from the European Union's Horizon 2020 research and innovation programme under grant agreement No 681002 (EU-ToxRisk; to J.B.B. and B.v.d.W.).

AUTHOR CONTRIBUTIONS

H.Y., M.N., B.v.d.W., and J.B.B. designed the research; H.Y. and M.N. performed the research; H.Y. and M.N. analyzed data; and H.Y., M.N., B.v.d.W., and J.B.B. wrote the paper.

DECLARATION OF INTERESTS

The authors declare no competing interests.

Received: August 16, 2019
Revised: December 9, 2019
Accepted: January 16, 2020
Published: February 21, 2020

REFERENCES

Ameri, K., and Harris, A.L. (2008). Activating transcription factor 4. Int. J. Biochem. Cell Biol. *40*, 14–21.

Braakman, I., and Hebert, D.N. (2013). Protein folding in the endoplasmic reticulum. Cold Spring Harbor Perspect. Biol. *5*, a013201.

Calfon, M., Zeng, H., Urano, F., Till, J.H., Hubbard, S.R., Harding, H.P., Clark, S.G., and Ron, D. (2002). IRE1 couples endoplasmic reticulum load to secretory capacity by processing the XBP-1 mrna. Nature *415*, 92.

Carrara, M., Prischi, F., Nowak, P.R., Kopp, M.C., and Ali, M.M. (2015). Noncanonical binding of BiP ATPase domain to Ire1 and Perk is dissociated by unfolded protein CH1 to initiate ER stress signaling. Elife *4*, e03522.

Chen, X., Shen, J., and Prywes, R. (2002). The lumenal domain of ATF6 senses ER stress and causes translocation of ATF6 from the ER to the Golgi. J. Biol. Chem. *277*, 13045–13052.

Chevet, E., Hetz, C., and Samali, A. (2015). Endoplasmic reticulum stress–activated cell reprogramming in oncogenesis. Cancer Discov. *5*, 586–597.

Cho, H., Wu, M., Zhang, L., Thompson, R., Nath, A., and Chan, C. (2013). Signaling dynamics of palmitate-induced ER stress responses mediated by atf4 in hepg2 cells. BMC Syst. Biol. *7*, 9.

Diedrichs, D.R., Gomez, J.A., Huang, C.S., Rutkowski, D.T., and Curtu, R. (2018). A data-entrained computational model for testing the regulatory logic of the vertebrate unfolded protein response. Mol. Biol. Cell *29*, 1502–1517.

Erguler, K., Pieri, M., and Deltas, C. (2013). A mathematical model of the unfolded protein stress response reveals the decision mechanism for recovery, adaptation and apoptosis. BMC Syst. Biol. *7*, 16.

Fredriksson, L., Wink, S., Herpers, B., Benedetti, G., Hadi, M., Bont, H.d., Groothuis, G., Luijten, M., Danen, E., Graauw, M.d., et al. (2014). Drug-induced endoplasmic reticulum and oxidative stress responses independently sensitize toward tnfα-mediated hepatotoxicity. Toxicol. Sci. *140*, 144–159.

Han, J., Back, S.H., Hur, J., Lin, Y.H., Gildersleeve, R., Shan, J., Yuan, C.L., Krokowski, D., Wang, S., Hatzoglou, M., et al. (2013). ER-stress-induced transcriptional regulation increases protein synthesis leading to cell death. Nat. Cell Biol. *15*, 481.

Harding, H.P., Novoa, I., Zhang, Y., Zeng, H., Wek, R., Schapira, M., and Ron, D. (2000). Regulated translation initiation controls stress-induced gene expression in mammalian cells. Mol. Cell *6*, 1099–1108.

Harding, H.P., Zhang, Y., and Ron, D. (1999). Protein translation and folding are coupled by an endoplasmic-reticulum-resident kinase. Nature *397*, 271.

Hartung, T., FitzGerald, R.E., Jennings, P., Mirams, G.R., Peitsch, M.C., Rostami-Hodjegan, A., Shah, I., Wilks, M.F., and Sturla, S.J. (2017).

Systems toxicology: real world applications and opportunities. Chem. Res. Toxicol. *30*, 870–882.

Hetz, C., and Papa, F.R. (2017). The unfolded protein response and cell fate control. Mol. Cell *169*, 169–181.

Ji, C., Mehrian-Shai, R., Chan, C., Hsu, Y.H., and Kaplowitz, N. (2005). Role of CHOP in hepatic apoptosis in the murine model of intragastric ethanol feeding. Alcohol. Clin. Exp. Res. *29*, 1496–1503.

Kuijper, I.A., Yang, H., Van De Water, B., and Beltman, J.B. (2017). Unraveling cellular pathways contributing to drug-induced liver injury by dynamical modeling. Expert Opin. Drug Metab. Toxicol. *13*, 5–17.

Lee, A.H., Iwakoshi, N.N., and Glimcher, L.H. (2003). XBP-1 regulates a subset of endoplasmic reticulum resident chaperone genes in the unfolded protein response. Mol. Cell Biol. *23*, 7448–7459.

Lu, P.D., Harding, H.P., and Ron, D. (2004). Translation reinitiation at alternative open reading frames regulates gene expression in an integrated stress response. J. Cell Biol. *167*, 27–33.

Ma, Y., Brewer, J.W., Diehl, J.A., and Hendershot, L.M. (2002). Two distinct stress signaling pathways converge upon the CHOP promoter during the mammalian unfolded protein response. J. Mol. Biol. *318*, 1351–1365.

Marciniak, S.J., Yun, C.Y., Oyadomari, S., Novoa, I., Zhang, Y., Jungreis, R., Nagata, K., Harding, H.P., and Ron, D. (2004). CHOP induces death by promoting protein synthesis and oxidation in the stressed endoplasmic reticulum. Genes Dev. *18*, 3066–3077.

Oda, Y., Okada, T., Yoshida, H., Kaufman, R.J., Nagata, K., and Mori, K. (2006). Derlin-2 and Derlin-3 are regulated by the mammalian unfolded protein response and are required for ER-associated degradation. J. Cell Biol. *172*, 383–393.

Oikawa, D., Kimata, Y., Kohno, K., and Iwawaki, T. (2009). Activation of mammalian IRE1α upon ER stress depends on dissociation of BiP rather than on direct interaction with unfolded proteins. Exp. Cell Res. *315*, 2496–2504.

Oppelt, A., Kaschek, D., Huppelschoten, S., Sison-Young, R., Zhang, F., Buck-Wiese, M., Herrmann, F., Malkusch, S., Krüger, C.L., Meub, M., et al. (2018). Model-based identification of TNFα-induced IKKβ-mediated and IκBα-mediated regulation of NFκB signal transduction as a tool to quantify the impact of drug-induced liver injury compounds. NPJ Syst. Biol. Appl. *4*, 23.

Oyadomari, S., and Mori, M. (2004). Roles of CHOP/GADD153 in endoplasmic reticulum stress. Cell Death Differ. *11*, 381.

Pawitan, Y. (2001). In All Likelihood: Statistical Modelling and Inference Using Likelihood (Oxford University Press).

Pincus, D., Chevalier, M.W., Aragón, T., Van Anken, E., Vidal, S.E., El-Samad, H., and Walter, P. (2010). BiP binding to the er-stress sensor Ire1 tunes the homeostatic behavior of the unfolded protein response. PLoS Biol. *8*, e1000415.

Poser, I., Sarov, M., Hutchins, J.R., Hériché, J.K., Toyoda, Y., Pozniakovsky, A., Weigl, D., Nitzsche, A., Hegemann, B., Bird, A.W., et al. (2008). Bac transgeneomics: a high-throughput method for exploration of protein function in mammals. Nat. Methods *5*, 409.

Ren, Z., Chen, S., Zhang, J., Doshi, U., Li, A.P., and Guo, L. (2016). Endoplasmic reticulum stress induction and ERK1/2 activation contribute to nefazodone-induced toxicity in hepatic cells. Toxicol. Sci. *154*, 368–380.

Rutkowski, D.T., Arnold, S.M., Miller, C.N., Wu, J., Li, J., Gunnison, K.M., Mori, K., Akha, A.A.S., Raden, D., and Kaufman, R.J. (2006). Adaptation to ER stress is mediated by differential stabilities of pro-survival and pro-apoptotic mrnas and proteins. PLoS Biol. *4*, e374.

Scheuner, D., Song, B., McEwen, E., Liu, C., Laybutt, R., Gillespie, P., Saunders, T., Bonner-Weir, S., and Kaufman, R.J. (2001). Translational control is required for the unfolded protein response and in vivo glucose homeostasis. Mol. Cell *7*, 1165–1176.

Shaffer, A., Shapiro-Shelef, M., Iwakoshi, N.N., Lee, A.H., Qian, S.B., Zhao, H., Yu, X., Yang, L., Tan, B.K., Rosenwald, A., et al. (2004). XBP1, downstream of Blimp-1, expands the secretory apparatus and other organelles, and increases protein synthesis in plasma cell differentiation. Immunity *21*, 81–93.

Shen, J., Chen, X., Hendershot, L., and Prywes, R. (2002). ER stress regulation of ATF6 localization by dissociation of BiP/GRP78 binding and unmasking of Golgi localization signals. Dev. Cell *3*, 99–111.

Sundaram, A., Appathurai, S., Plumb, R., and Mariappan, M. (2018). Dynamic changes in complexes of IRE1α, PERK, and ATF6 α during the endoplasmic reticulum stress. Mol. Biol. Cell *29*, 1376–1388.

Takayanagi, S., Fukuda, R., Takeuchi, Y., Tsukada, S., and Yoshida, K. (2013). Gene regulatory network of unfolded protein response genes in endoplasmic reticulum stress. Cell Stress Chaperones *18*, 11–23.

Trusina, A., Papa, F.R., and Tang, C. (2008). Rationalizing translation attenuation in the network architecture of the unfolded protein response. Proc. Natl. Acad. Sci. U S A *105*, 20280–20285.

Trusina, A., and Tang, C. (2010). The unfolded protein response and translation attenuation: a modelling approach. Diabetes Obes. Metab. *12*, 27–31.

Urra, H., Dufey, E., Lisbona, F., Rojas-Rivera, D., and Hetz, C. (2013). When ER stress reaches a dead end. Biochim. Biophys. Acta *1833*, 3507–3517.

Uzi, D., Barda, L., Scaiewicz, V., Mills, M., Mueller, T., Gonzalez-Rodriguez, A., Valverde, A.M., Iwawaki, T., Nahmias, Y., Xavier, R., et al. (2013). CHOP is a critical regulator of acetaminophen-induced hepatotoxicity. J. Hepatol. *59*, 495–503.

Vitale, M., Bakunts, A., Orsi, A., Lari, F., Tadè, L., Danieli, A., Rato, C., Valetti, C., Sitia, R., Raimondi, A., et al. (2019). Inadequate bip availability defines endoplasmic reticulum stress. Elife *8*, e41168.

Wang, M., and Kaufman, R.J. (2016). Protein misfolding in the endoplasmic reticulum as a conduit to human disease. Nature *529*, 326.

Wink, S., Hiemstra, S., Herpers, B., and van de Water, B. (2017). High-content imaging-based bac-gfp toxicity pathway reporters to assess chemical adversity liabilities. Arch. Toxicol. *91*, 1367–1383.

Wink, S., Hiemstra, S.W., Huppelschoten, S., Klip, J.E., and van de Water, B. (2018). Dynamic imaging of adaptive stress response pathway activation for prediction of drug induced liver injury. Arch. Toxicol. *92*, 1797–1814.

Wu, J., Rutkowski, D.T., Dubois, M., Swathirajan, J., Saunders, T., Wang, J., Song, B., Yau, G.D.Y., and Kaufman, R.J. (2007). Atf6α optimizes long-term endoplasmic reticulum function to protect cells from chronic stress. Dev. Cell *13*, 351–364.

Yamamoto, K., Sato, T., Matsui, T., Sato, M., Okada, T., Yoshida, H., Harada, A., and Mori, K. (2007). Transcriptional induction of mammalian ER quality control proteins is mediated by single or combined action of ATF6α and XBP1. Dev. Cell *13*, 365–376.

Ye, J., Rawson, R.B., Komuro, R., Chen, X., Davé, U.P., Prywes, R., Brown, M.S., and Goldstein, J.L. (2000). ER stress induces cleavage of membrane-bound ATF6 by the same proteases that process srebps. Mol. Cell *6*, 1355–1364.

Yoo, J., Mashalidis, E.H., Kuk, A.C., Yamamoto, K., Kaeser, B., Ichikawa, S., and Lee, S.Y. (2018). GlcNAc-1-P-transferase–tunicamycin complex structure reveals basis for inhibition of N-glycosylation. Nat. Struct. Mol. Biol. *25*, 217.

Yoshida, H., Matsui, T., Hosokawa, N., Kaufman, R.J., Nagata, K., and Mori, K. (2003). A time-dependent phase shift in the mammalian unfolded protein response. Dev. Cell *4*, 265–271.

Yoshida, H., Matsui, T., Yamamoto, A., Okada, T., and Mori, K. (2001). XBP1 mRNA is induced by ATF6 and spliced by IRE1 in response to ER stress to produce a highly active transcription factor. Cell *107*, 881–891.

Yoshida, H., Okada, T., Haze, K., Yanagi, H., Yura, T., Negishi, M., and Mori, K. (2000). ATF6 activated by proteolysis binds in the presence of NF-Y (CBF) directly to the cis-acting element responsible for the mammalian unfolded protein response. Mol. Cell Biol. *20*, 6755–6767.

iScience, Volume *23*

Supplemental Information

ATF6 Is a Critical Determinant of CHOP Dynamics during the Unfolded Protein Response

Huan Yang, Marije Niemeijer, Bob van de Water, and Joost B. Beltman

Supplemental data items

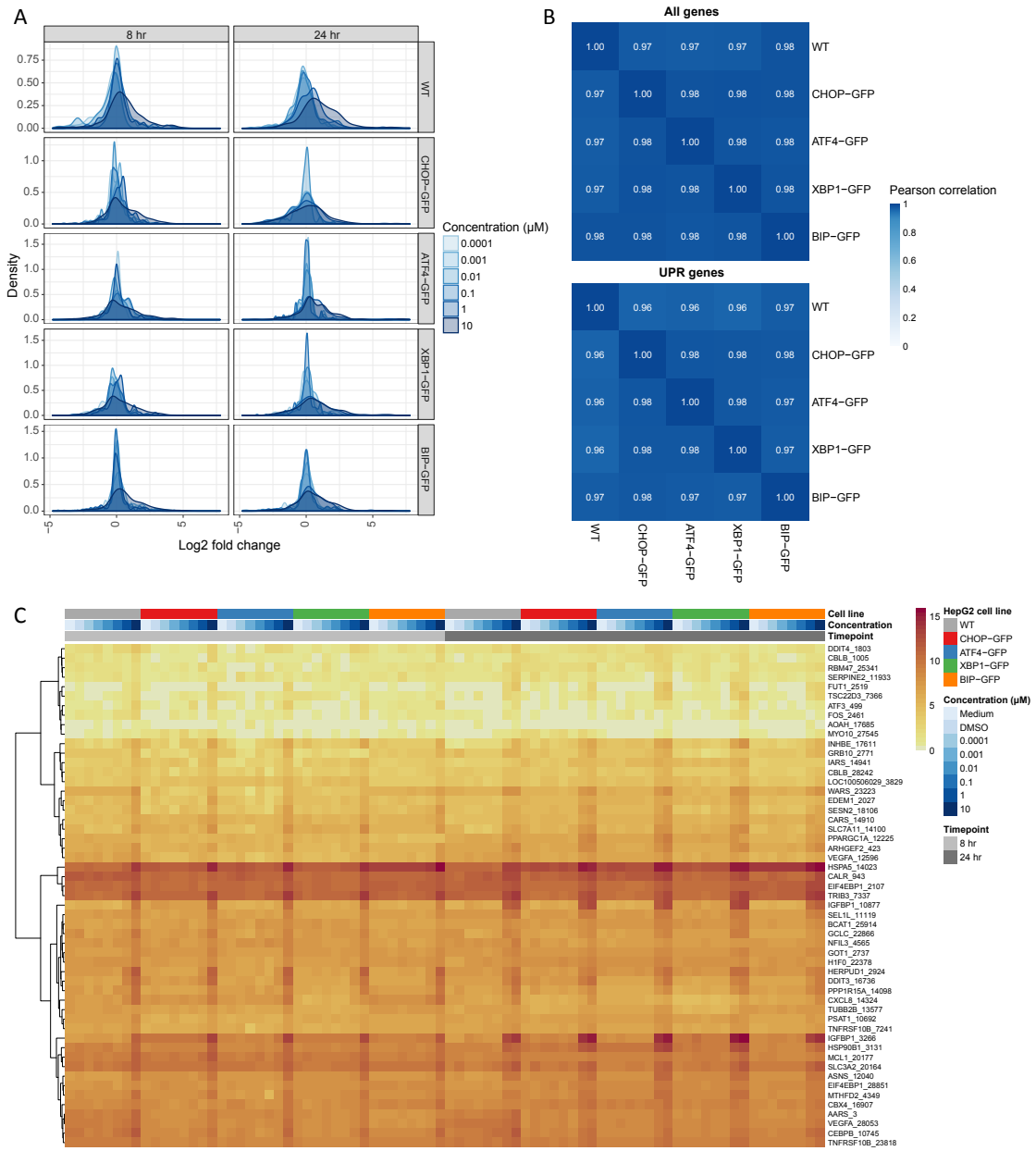

Figure S1: **Transcriptomic profiling of HepG2 UPR BAC-GFP reporters, related to Figure 2**. **A**: Distribution of log2 fold changes (compared to DMSO solvent control) of UPR-related genes across the indicated concentration range of tunicamycin for each HepG2 cell line (WT, CHOP-GFP, ATF4-GFP, pXBP1(S)-GFP and BiP-GFP) at 8 and 24h exposure time. **B**: Pearson correlation matrix of different HepG2 cell lines based on either all genes (top panel) or UPR-related genes (lower panel). Correlations are the mean of correlations between cell lines at each concentration of tunicamycin. **C**: Heatmap of log2 normalized counts of UPR-related genes (selection based on upper quantile of log2 fold changes of all UPR-related genes at 10 μM) for each HepG2 cell line exposed to the indicated concentration range of tunicamycin either for 8 or 24h. Hierarchical clustering of genes based on euclidean distance.

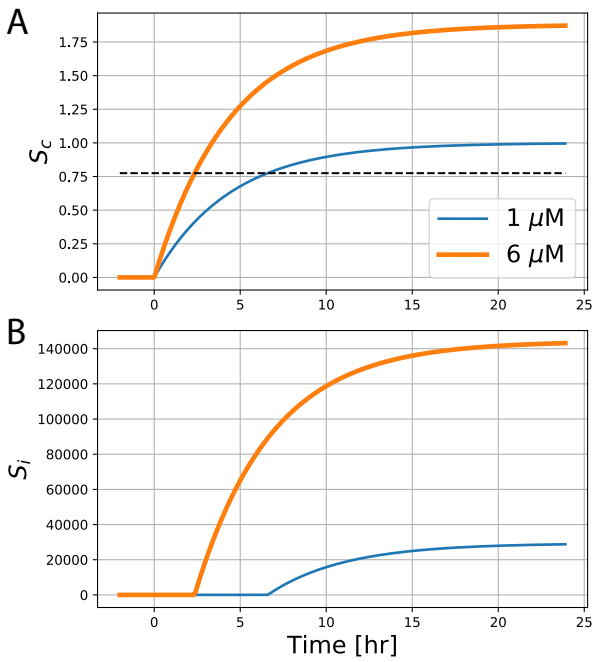

Figure S2: **Modeled pharmacokinetics of tunicamycin exposure, related to Figure 2 and 3**. **A**: effective intra-cellular concentration of tunicamycin S_c over time, **B**: exposure-related stressor S_i (unfolded proteins due to tunicamycin) which acts as input to the UPR signaling network.

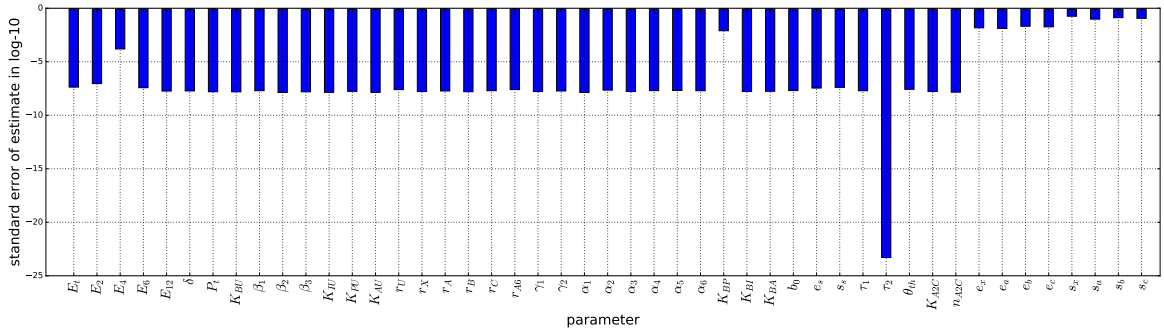

Figure S3: **Standard errors of model parameter estimates, related to Figure 3**. The standard errors were approximated via a Hessian-based approach and are presented in log10 scale.

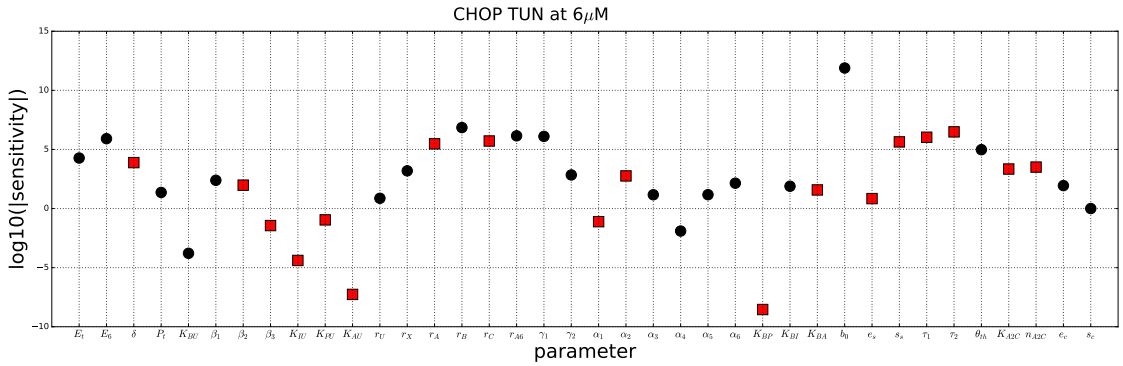

Figure S4: **Parameter sensitivity analysis of CHOP expression, related to Figure 3**. In the sensitivity analysis, we considered the sensitivity of CHOP expression at 16 hours after exposure to 6μM of tunicamycin. Parameters positively affecting CHOP are shown in black, while parameters negatively affecting CHOP are shown in red.

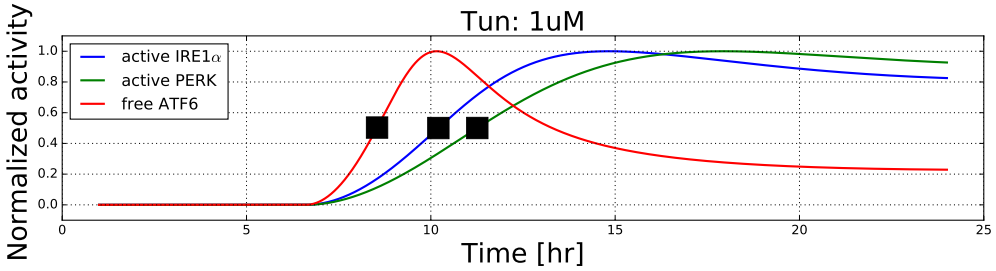

Figure S5: **Predicted dynamics of the three UPR sensors upon tunicamycin exposure, related to Figure 4**. Plot of the dynamics of the sensors IRE1α (blue), PERK (green), and ATF6 (red), after normalization to their maximally obtained value during the studies time period. Black squares indicate the moment at which sensor activity is half-maximal.

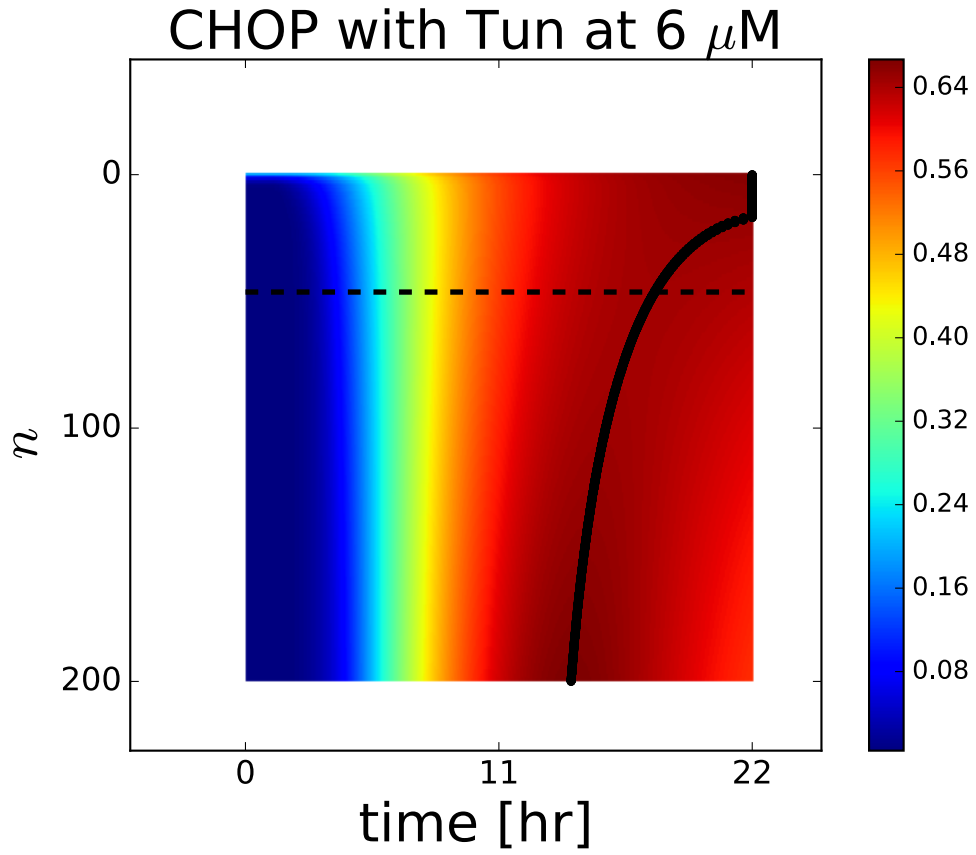

Figure S6: **Effect of n on CHOP upon exposure to 6 μM of tunicamycin, related to Figure 4**. Heat-map showing the temporal response of CHOP for a range of n values. The black solid line indicates the time point of maximal CHOP activity within the simulated time period. The black dashed line indicates the best fit value ($n = 46.32$).

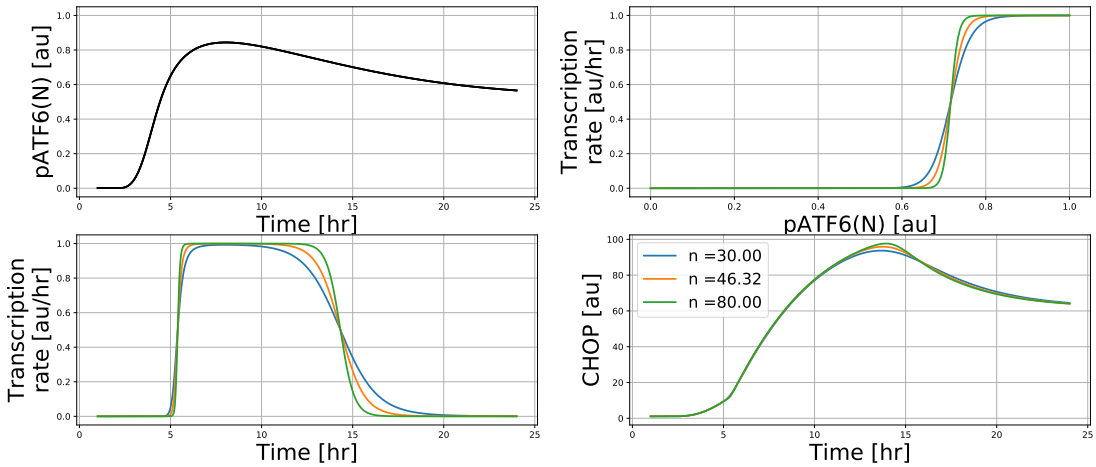

Figure S7: **Sensitivity of the CHOP response to the Hill coefficient describing the relation with pATF6(N), related to Figure 4**. For three values of n (including the estimated value of $n = 46.32$), we plot the pATF6(N) response over time (upper left panel), the relation between CHOP transcription and pATF6(N) level (upper right panel), the CHOP transcription rate due to pATF6(N) over time (lower left panel) and CHOP dynamics (lower right panel).

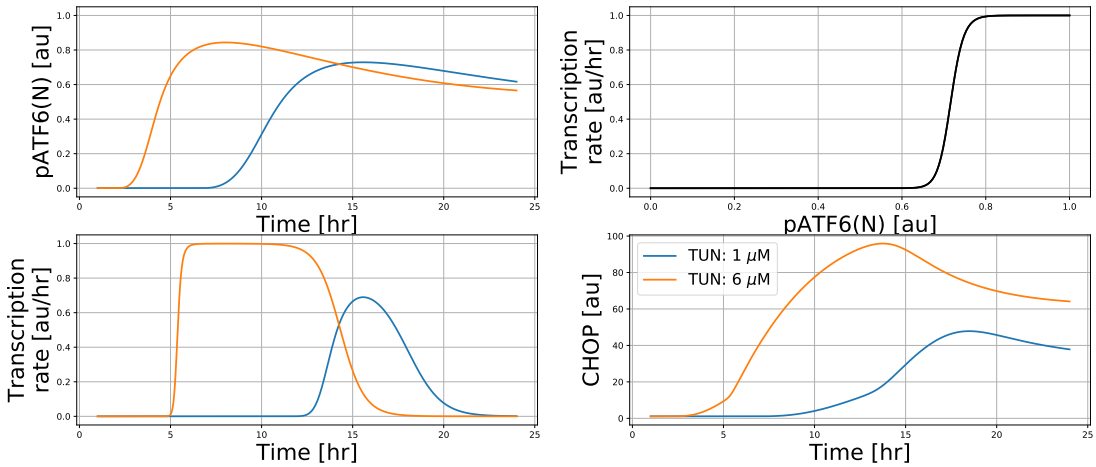

Figure S8: **Details of inner model states with respect to the CHOP response at different tunicamycin concentrations, related to Figure 4**. For two tunicamycin concentrations, we plot the pATF6(N) response over time (upper left panel), the relation between CHOP transcription and pATF6(N) level (upper right panel), the CHOP transcription rate due to pATF6(N) over time (lower left panel) and CHOP dynamics (lower right panel).

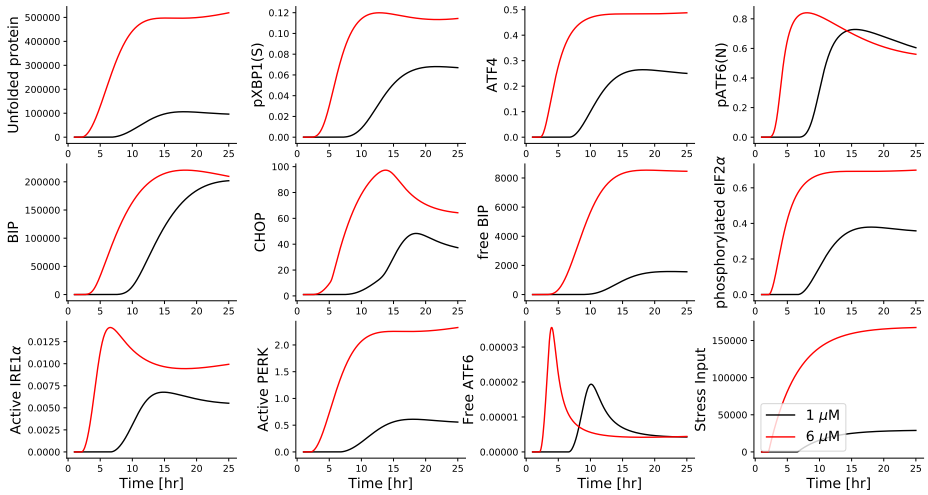

Figure S9: **Simulation of inner model states, related to Figure 3 and 4**. Dynamics of modeled UPR network components are shown upon exposure to tunicamycin at 1μM (black) and 6μM (red). Note that free ATF6 stands for activated ATF6 sensor, i.e., free uncleaved ATF6. Among the three branches, ATF4 tightly follows the dynamics of eIF2α_p and unfolded proteins.

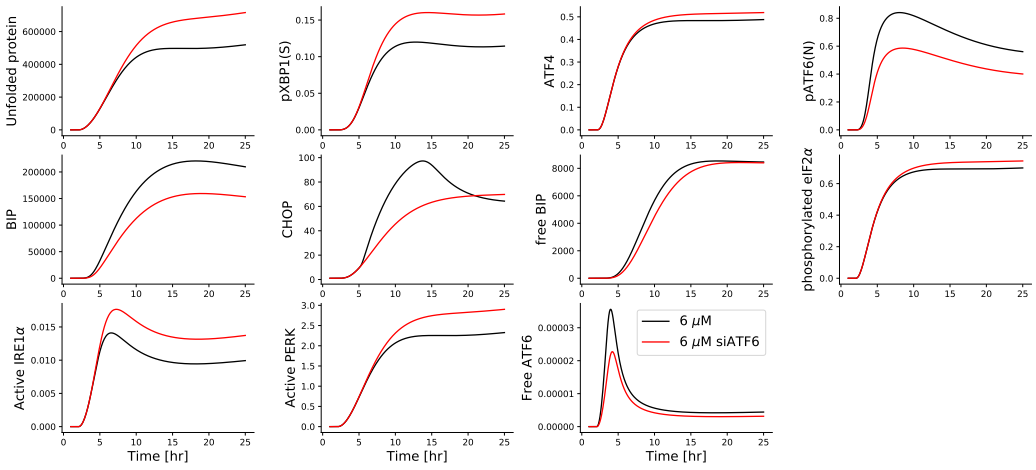

Figure S10: **Simulation of inner model states upon ATF6 knockdown, related to Figure 3 and 5**. Dynamics of modeled UPR network components upon exposure to 6μM tunicamycin, either with (red) or without (black) siATF6 treatment. Note that siATF6 results in lower BiP levels, which reduces the folding capacity. Hence, there are more unfolded proteins, which induces more ATF4 and pXBP1(S), in the long run leading to slightly higher CHOP levels compared to a setting without siATF6.

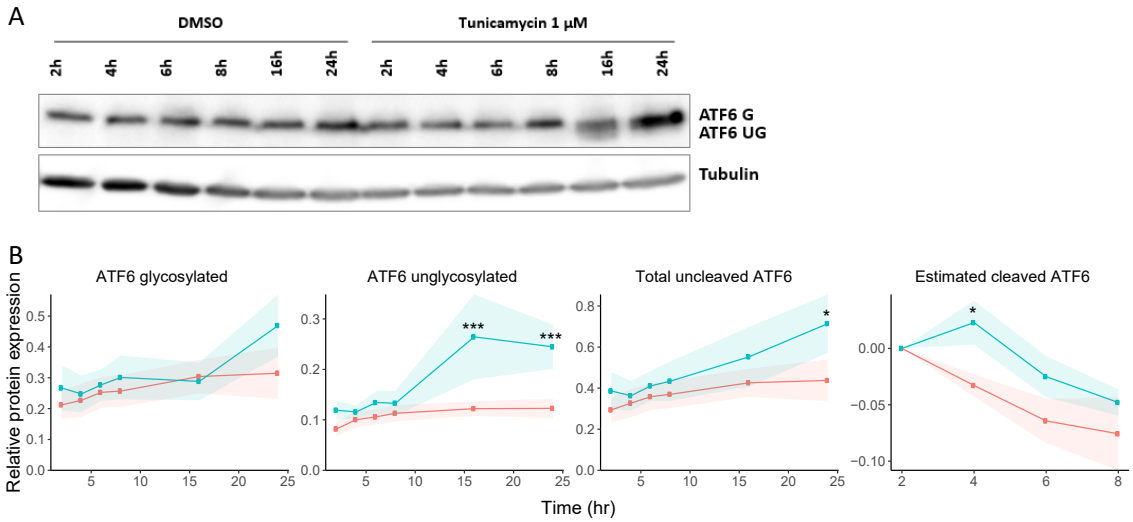

Figure S11: **Quantification of ATF6 forms after treatment of 1 μM tunicamycin, related to Figure 6**. **A**: Western blot of uncleaved ATF6 (G = glycosylated, UG = unglycosylated) measured in HepG2 WT cells at 2, 4, 6, 8, 16 or 24 hours after exposure to tunicamycin (1 μM). Tubulin protein expression was used as protein loading control. **B**: Quantified protein expression of ATF6 forms from three biological replicates after protein loading correction using tubulin (symbols and shaded area represent mean ± SD). Cleaved ATF6 was estimated based on the difference between total uncleaved ATF6 at 4, 6, or 8h and the total ATF6 at 2h.

Table S1: Model parameters, their units, their estimated values (± 95% confidence interval) and the boundary values used during the estimation procedure, related to Figure 3, 4, 5 and 6. For the rationale behind the choice of boundary values see the section on parameter ranges.

Parameter	unit	description	estimated $\boldsymbol{\theta_1}$	estimated $\boldsymbol{\theta_2}$ ± 95% CI	lower boundary	upper boundary
E_t	-	general translation rate (from mRNA to unfolded protein)	2.21e+00	2.00e+00 ± 8.45e-08	1.0	200.0
E_2	au	effective exposure at 2 μM	1.16e+00	1.22e+00 ± 1.80-e07	1.0	20.0
E_4	au	effective exposure at 4 μM	1.55e+00	1.67e+00± 3.10e-04	1.0	20.0
E_6	au	effective exposure at 6 μM	1.88e+00	2.07e+00 ± 7.45e-08	1.0	20.0
E_{12}	au	effective exposure at 12 μM	2.11e+00	2.48e+00± 3.62e-08	1.0	20.0
δ	au/hr	BiP-mediated folding rate	1.84e+01	1.96e+01 ± 3.70e-08	0.10	200.0
P_t	-	total amount of PERK	1.87e+01	8.36e+00 ± 3.12e-08	1.0	2.0e5
K_{BU}	au	Michaelis-Menten constant for dissociation of BiP and unfolded proteins	1.24e+07	1.24e+07 ± 3.07e-08	1e3	1e10
β_1	au/hr	IRE1α-dependent formation rate of XBP1	4.90e+00	2.75e+00 ± 3.90e-08	1.0e-8	2.0e8
β_2	au/hr	PERK-dependent ATF4 formation rate	1.52e+01	4.35e+00 ± 2.67e-08	1.0e-8	2.0e8
β_3	au/hr	ATF6-dependent ATF6f formation rate	-	1.18e+04 ± 3.08e-08	1.0e-8	2.0e8
K_{IU}	au	Michaelis-Menten constant for dissociation of IRE1α and unfolded proteins	9.57e+06	9.56e+06 ± 2.75e-08	1e1	1e10
K_{PU}	au	Michaelis-Menten constant for dissociation of PERK and unfolded proteins	1.35e+06	1.35e+06 ± 3.42e-08	1e1	1e10
K_{AU}	au	Michaelis-Menten constant for dissociation of ATF6 and unfolded proteins	-	1.08e+09 ± 2.71e-08	1e1	1e10
r_U	1/hr	degradation rate of unfolded proteins	4.07e-02	2.02e-08 ± 4.95e-08	1.0e-8	2.0e3
r_X	1/hr	degradation rate of XBP1	5.16e-01	2.34e-01± 3.29e-08	1.0e-8	2.0e3
r_{A_4}	1/hr	degradation rate of ATF4	4.95e+00	6.26e+00± 3.68e-08	1.0e-8	2.0e3
r_B	1/hr	degradation rate of BiP	2.58e-01	1.52e-01± 3.14e-08	1.0e-8	2.0e3
r_C	1/hr	degradation rate of CHOP	9.95e-01	2.83e-0± 3.92e-08	1.0e-8	2.0e3
r_{A_6}	1/hr	degradation rate of ATF6f	-	1.05e-0± 4.96e-08	1.0e-8	2.0e3
γ_1	au/hr	basal BiP transcription rate	1.13e+00	6.25e-01± 3.26e-08	0	2e2
γ_2	au/hr	basal CHOP transcription rate	3.29e-01	2.96e-01± 3.68e-08	0	2e2
α_1	1/hr	XBP1-mediated BiP transcription rate	8.14e+04	8.14e+0± 2.68e-08	0	1e6
α_2	1/hr	ATF4-mediated BiP transcription rate	2.97e+03	2.60e+02± 4.43e-08	0	1e6
α_3	1/hr	XBP1-mediated CHOP transcription rate	3.15e+02	3.17e+01± 3.26e-08	0	1e6
α_4	1/hr	ATF4-mediated CHOP transcription rate	2.86e+02	2.88e+01± 3.94e-08	0	1e6
α_5	1/hr	ATF6f-mediated BiP transcription rate	-	5.09e+04± 4.08e-08	0	1e6
α_6	au/hr	ATF6f-mediated CHOP transcription rate	-	1.39e+01± 3.87e-08	0	1e6
K_{BP}	au	Michaelis-Menten constant for dissociation of BiP and PERK	5.03e+07	5.03e+07± 1.56e-02	0	1e9
K_{BI}	au	Michaelis-Menten constant for dissociation of BiP and IRE1α	8.81e+02	1.92e+03± 3.27e-08	0	1e9
K_{BA}	au	Michaelis-Menten constant for dissociation of BiP and ATF6	-	7.81e+01± 3.45e-08	0	1e9
b_0	au/hr	basal production rate of ATF4	2.91e-06	2.41e-06± 4.00e-08	0	2e2
e_s	au/hr	factor scaling the effective intra-cellular concentration to unfolded proteins	1.31e+05	1.31e+05± 6.88e-08	1e-3	2e7
s_s	au/hr	net production rate of unfolded proteins independent of translation attenuation and exposure	-1.870	-2.00 ± 8.01e-08	-20.0	2e3
τ_1	1/hr	time constant describing initial increase in stressor	2.47e-01	2.26e-01± 3.87e-08	1e-15	5.0
τ_2	1/hr	time constant describing stressor decay	8.90e-03	8.45e-15± 1.01e-23	1e-15	5.0
θ_{th}	au	threshold for stressor levels that activate signaling	7.37e-01	7.75e-01 ± 5.29e-08	0.0	1.0
K_{A2C}	au	ATF6f level at which ATF6f-dependent CHOP transcription is half-maximal	-	7.17e-01± 3.32e-08	1e-8	1e4
n	-	cooperativity in ATF6f-dependent CHOP transcription Hill kinetics	-	4.63e+01± 2.86e-08	1e-2	1.0e2
e_{XBP1}	au	GFP scaling factor for XBP1 reporters	5.64	6.60± 2.94e-02	1.0e-7	1.0e2
e_{ATF4}	au	GFP scaling factor for ATF4 reporters	2.28e-01	1.23e+00± 2.58e-02	1.0e-7	1.0e2
e_{BIP}	au	GFP scaling factor for BiP reporters	1.13e-05	3.68e-06± 4.12e-02	1.0e-7	1.0e2
e_{CHOP}	au	GFP scaling factor for CHOP reporters	1.45e-02	7.75e-03± 3.60e-02	1.0e-7	1.0e2
s_{XBP1}	au	GFP offset for XBP1 reporters	5.20e-04	5.65e-04 ± 3.55e-01	-1.0e2	1.0e2
s_{ATF4}	au	GFP offset for ATF4 reporters	3.54e-02	4.19e-02± 1.90e-01	-1.0e2	1.0e2
s_{BIP}	au	GFP offset for BiP reporters	1.09e-01	7.81e-02± 2.61e-01	-1.0e2	1.0e2
s_{CHOP}	au	GFP offset for CHOP reporters	-7.10e-04	-3.89e-03 ± 2.26e-01	-1.0e2	1.0e2

Transparent Methods

Experimental details

Cell culture

HepG2 human hepatocellular carcinoma cells were purchased at American Type Culture Collection (ATCC, Wesel, Germany). To capture the induction of key proteins of the UPR, CHOP, ATF4, BiP and pXBP1(S) were GFP-tagged using a bacterial artificial chromosome (BAC) recombineering approach (Poser et al., 2008; Wink et al., 2014; Hendriks et al., 2011; Wink et al., 2017; Hiemstra et al., 2016). Hereby, stable HepG2 GFP-BAC reporter cell lines were established expressing protein-GFP fusions under control of the endogenous promoter for each gene. HepG2 cells were cultured in Dulbecco's Modified Eagle Medium (DMEM) containing 10% (v/v) fetal bovine serum (FBS), 25 U/mL penicillin and 25 μg/mL streptomycin at 37°C and 5% CO_2, and were used until passage 20. Cells were plated using a density of 70.000 to 140.000 cells/cm^2 when grown for 3 to 5 days.

Chemicals and antibodies

Tunicamycin was purchased at Sigma (Zwijndrecht, The Netherlands) which was dissolved in dimethylsulfoxide (DMSO) from BioSolve (Valkenswaard, The Netherlands) and stored at -20°C until usage. The maximum solvent end concentration of DMSO was at most 0.2% (v/v) to minimize the effect of the solvent itself. For western blotting, antibodies were used against CHOP, ATF4, pXBP1(S) and ATF6 from Cell Signaling (Bioké, Leiden, The Netherlands), BiP from BD Biosciences (Vianen, The Netherlands) at a dilution of 1:1000, and Tubulin from Sigma (Zwijndrecht, The Netherlands) at a dilution of 1:5000.

RNA interference

siRNA-mediated transient silencing of genes of interest in HepG2 cells was done using a reverse transfection approach. Prior to transfection, siGENOME SMARTpool siRNAs from Dharmacon (Eindhoven, the Netherlands) were mixed with INTERFERin from PolyPlus (Leusden, the Netherlands) for 10 minutes to allow for complex formation. Hereafter, siRNA mix, resulting in a 50 nM siRNA and 0.3% INTERFERin end concentration, together with cells at a density of 78.000 cells/cm^2 were added to each well. As control, mock (only INTERFERin) and siRNA scrambled non-targeting control was employed. At 24 hours post-transfection, medium was refreshed. siRNA-silenced cells were evaluated at 72 hours post transfection or exposed to compounds to assess the effect of the knockdown on drug-induced ER stress response activation.

Confocal Microscopy

Cells were plated in SCREENSTAR 96 wells or μClear 384 wells plates from Greiner Bio-One (Alphen aan den Rijn, The Netherlands) at the earlier mentioned cell densities. Prior to confocal microscopy imaging, cells were stained with 100 ng/mL Hoechst33342 for a minimum of 30 minutes to allow for nuclei visualization and cell tracking. To measure the induction of BAC-GFP intensity, cells were imaged live using an automated Nikon TiE2000 confocal microscope (Nikon, Amsterdam, The Netherlands) including an automated xy-stage, Perfect Focus System and lasers at wavelength 408, 488, 561 and 647nm. Cells were kept at 37°C and 5% CO2 humidified atmosphere during imaging.

Image Analysis

Segmentation and quantification of the GFP intensity was done using CellProfiler version 2.1.1 (Broad Institute Cambridge, USA) using analysis modules described previously (Wink et al., 2014; Niemeijer et al., 2018). In brief, nuclear segmentation based on Hoechst signal was done using an in-house constructed watershed masking algorithm (Di et al., 2012). The propagation

segmentation method based on GFP signal was used for cytoplasm segmentation. GFP intensity was measured in the nucleus as well as in the cytoplasm. For subsequent analysis, Rstudio version 1.0.153 (Boston, USA) was used. For alignment of the data acquired around discrete time points (1,2,..., 24 hours), we employed cubic interpolation of the GFP intensity such that standard deviations can be estimated from the individual replicates, which are integrated into the cost function for parameter estimation (see Supplementary text about single-cell data analysis for details).

TempO-seq transcriptomics

To assess mRNA levels, cells were seeded in 96 wells plates from Corning (Amsterdam, The Netherlands) using a density of 156.000 cells/cm^2. After compound exposure the following day, cells were washed with 1x PBS and lysed using 50 μL per well in 1x BNN lysis buffer from BioSpyder (Carlsbad, USA). After a 15 minute incubation period at room temperature, lysates were frozen at -80°C. As internal control, 0.05 μg/μL Universal Human RNA Reference (MAQC) in 1x BNN lysis buffer was used. Lysates were sent to and analyzed by BioSpyder Technologies Inc. (Carlsbad, USA) using the TempO-seq technology (Yeakley et al., 2017) of a targeted gene set consisting of the S1500+ gene list (Mav et al., 2018). In brief, a pair of detector oligos hybridized to its specific target mRNA leading to oligo pair ligation. This was followed by PCR amplification of ligated pairs of oligos incorporating also a sample-barcode and adaptors, which was subsequently sequenced. Alignment of raw reads was done using the TempO-seqR package (BioSpyder Technologies Inc., Carlsbad, USA). Read counts were normalized using the DESeq2 R package (Love et al., 2014) and log2 transformed. UPR-related genes were defined by selecting target genes of transcription factors ATF4, ATF6, pXBP1(S) and DDIT3 that were based on DoRothEA (Discriminant Regulon Expression Analysis) v2 (Garcia-Alonso et al., 2018) using confidence level A to D and that were present in the S1500+ geneset.

Western blot analysis

For western blot analysis, samples were collected after two wash steps with ice-cold 1x PBS by adding 1x sample buffer supplemented with 10% v/v β-mercaptoethanol and stored at -20°C. Prior to loading, samples were heat-denatured at 95°C for 10 minutes. Proteins were separated on SDS-page gels using 120 volt and transferred to polyvinylidene difluoride (PVDF) membranes at 100 volt for 2 hours. After blocking using 5% ELK, membranes were stained with primary and secondary HRP- or Cy5-conjugated antibodies diluted in 1% bovine serum albumin (BSA) in tris-buffered saline (TBS)-0.05%Tween20. Thereafter, Enhanced Chemiluminescent (ECL) western blotting substrate from Thermo Scientific (Bleiswijk, The Netherlands) enabled to visualize the HRP-conjugated antibody staining using the Amersham Imager 600 from GE Healthcare (Eindhoven, The Netherlands). Protein expression was quantified using ImageJ version 1.51h (National Institutes of Health, USA) and normalized to tubulin protein expression.

Statistics

Confocal microscopy data from three biological replicates is represented as the mean ± SE. TempO-seq gene expression data was represented either as log2 normalized counts ± SE or as log2 fold changes with standard error calculated using the DESeq2 R package (Love et al., 2014). Significance was determined with the Wald test and Benjamini Hochberg correction using the DESeq2 R package (Love et al., 2014). Significance for TempO-seq gene expression data was determined at three threshold levels ($^*p_{adj} < 0.05$, $^{**}p_{adj} < 0.01$, $^{***}p_{adj} < 0.001$). Western blot data for ATF6 quantification originated from three biological replicates and were represented as the mean ± SE. Here, significance levels were calculated using unpaired Student's t test with Benjamini Hochberg multiple testing correction, represented as $^*p_{adj} < 0.1$, $^{**}p_{adj} < 0.05$, $^{***}p_{adj} < 0.01$. Processing and visualization of all data was done using Rstudio version 1.0.153 (Boston, USA) in combination with R 3.4.1 and the following R packages: ggplot2 (Wickham, 2010), RColorBrewer

(Neuwirth, 2014), data.table (Dowle et al., 2018), dplyr (Wickham et al., 2011), tidyr (Wickham, 2017), reshape2 (Zhang, 2016), scales, stats and splines.

Computational modeling

UPR model construction and simulation

We built a dynamic model of the UPR signaling network with six state variables: unfolded protein (U), pXBP1(S) (X), ATF4 (A_4), ATF6 fragment(A_6), BiP (B), and CHOP (C). These states represent concentrations of molecules per cell and their dynamics are mathematically described by a set of ordinary differential equations. The equations obey kinetics of biochemical reactions including mass-action, Michaelis-Menten or Hill kinetics. We simplified the model in a similar way as (Trusina et al., 2008; Diedrichs et al., 2018) with quasi-steady state assumptions for association or dissociation of complexes and modulation effects. Furthermore, we took multiple conservation terms into account in order to reduce the number of state variables. We extended the available model of (Trusina et al., 2008) by incorporating ATF4 and CHOP. Furthermore, because ATF6 is proteolytically processed but this is not the case in the XBP1 branch (Ye et al., 2000), we considered the possibility that ATF6 and XBP1 need to be assigned different parameters (e.g., their degradation rates) to allow these branches to respond differently. To take the pharmacokinetics of the exposure into account, we modeled the intra-cellular concentration of tunicamycin as a function with two exponents, which represents the analytical solution to a linear system for two compartments (i.e., the medium in which cells reside and intra-cellular spaces).

The set of ODEs is mathematically represented as

$$\dot{\mathbf{x}}(t) = \mathbf{f}(\mathbf{x}(\mathbf{t}), \mathbf{u}(\mathbf{t}), \theta), \tag{1}$$

where $x(t)$ stands for the six state variables of the dynamic system, $u(t)$ is the input function, and θ contains the system parameters. The dynamics of the UPR state variables are described by:

$$\begin{cases} \dot{U} = f_1(x), \\ \dot{X} = f_2(x), \\ \dot{A}_4 = f_3(x), \\ \dot{A}_6 = f_4(x), \\ \dot{B} = f_5(x), \\ \dot{C} = f_6(x), \end{cases} \tag{2}$$

with initial condition

$$\mathbf{x}_0 = (U_0, X_0, A_{4,0}, A_{6,0}, B_0, C_0)^{\cdot} \tag{3}$$

In the following the right hand sides of equations (2) are provided for each state. Our modeling work follows (Trusina et al., 2008) assuming a quasi steady-state for sensors which can bind to BiP or to unfolded proteins. In addition, we incorporated the ATF6 branch and the downstream molecules ATF4 and CHOP (Trusina et al., 2008). This allows to integrate all experimental data obtained from our GFP reporter cell lines, i.e., pXBP1(S), ATF4, BiP and CHOP.

We subsequently describe all equations for the system states, starting with the unfolded protein U:

$$f_1(\mathbf{x}) = \frac{E_t}{1 + P_{act}} + s_s + S_i - \delta\, B_f - r_U\, U\,, \tag{4}$$

where E_t denotes the base rate of translation, i.e., the formation of peptides or unfolded proteins from mRNA which can be modulated by translation attenuation. S_i represents the rate of production of unfolded proteins due to the exposure-related stressor, which is described explicitly as

a function of time (see below). The parameter s_s represents a net folding/unfolding rate that is independent of BiP and of translation. Instead, it includes both the folding activity of chaperones other than BiP and unfolding activity of existing proteins. Because it represents a net effect, s_s can have a positive or negative value, depending on which process prevails. Unfolded proteins are removed by degradation, which occurs at rate r_U, or by their folding following binding to the chaperone BiP, which occurs at rate δ. The latter process depends on the amount of free form of BiP, which is given by

$$B_f = \frac{U}{U + K_{BU}}\, B\,, \tag{5}$$

where K_{BU} is the amount of unfolded proteins for which half of the BiP molecules is present in free form. Inhibition of translation is modeled by modification of the E_t term, where P_{act} denotes the active form of PERK and is given by

$$P_{act} = P_t\,(U/K_{PU})/(1 + B_f/K_{BP} + U/K_{PU})\,, \tag{6}$$

where P_t is the effective/net amount of PERK, and K_{PU} and K_{BP} are Michaelis-Menten parameters describing the affinity of the complexes PERK:UP and BiP:UP, respectively.

The amount of spliced XBP1 is described by:

$$f_2(\mathbf{x}) = \beta_1\, I_{act} - r_X\, X\,. \tag{7}$$

Here, β_1 represents the XBP1 splicing rate, which depends on the amount of active IRE1α. The latter is represented by I_{act} and is given by:

$$I_{act} = (U/K_{IU})/(1 + B_f/K_{BI} + U/K_{IU})\,, \tag{8}$$

where K_{IU} and K_{BI} are Michaelis-Menten parameters describing the affinity of the complexes IRE1α:UP and BiP:IRE1α, respectively. Spliced XBP1 is degraded at rate r_X.

The amount of ATF4 is described by:

$$f_3(\mathbf{x}) = b_0 + \beta_2\, eIF2\alpha_p - r_{A_4}\, A_4, \tag{9}$$

where r_{A_4} denotes the degradation rate of ATF4, b_0 indicates its basal production rate, and β_2 is the additional production rate of ATF4 due to $eIF2\alpha_p$, where eIF2α_p is the fraction of phosphorylated eIF2α that obeys:

$$eIF2\alpha_p = 1 - eIF2\alpha_{up} = 1 - \left(1 + \frac{P_t\, U}{K_{PU} + B_f\, K_{PU}/K_{BP} + U}\right)^{-1}, \tag{10}$$

where $eIF2\alpha_{up}$ denotes the fraction of unphosphorylated eIF2α. Note that the total amount of $eIF2\alpha$ (phosphorylated and unphosphorylated) is considered to be conserved.

The amount of pATF6(N) is described by:

$$f_4(\mathbf{x}) = \beta_3\, A_{6,act} - r_{A_6}\, A_6, \tag{11}$$

where $A_{6,act}$ is the activated sensor (i.e., the free form of ATF6, which is not the same as pATF6(N)), which obeys

$$A_{6,act} = (U/K_{AU})/(1 + B_f/K_{BA} + U/K_{AU})\,. \tag{12}$$

As before, K_{AU} and K_{BA} are Michaelis–Menten parameters representing the affinity of the complexes ATF6:UP and BiP:ATF6, respectively.

The amount of BiP is described by:

$$f_5(\mathbf{x}) = \gamma_1 + \alpha_1\, X + \alpha_2\, A_4 + \alpha_5\, A_6 - r_B\, B\,, \tag{13}$$

where γ_1 is the basal production rate of BiP, r_B is the degradation rate of BiP, and α_1, α_2, α_5 represent the additional BiP production rate due to activity of pXBP1(S), ATF4 and pATF6(N), respectively.

The amount of CHOP is described by:

$$f_6(\mathbf{x}) = \gamma_2 + \alpha_3\, X + \alpha_4\, A_4 + \alpha_6\, A_{6,hill} - r_C\, C, \tag{14}$$

where γ_2 is the basal production rate of CHOP, r_C is the degradation rate of CHOP, and α_3, α_4, α_6 represent the additional CHOP production rate due to activity of pXBP1(S), ATF4 and pATF6(N), respectively. $A_{6,hill}$ describes the contribution of pATF6(N) to the CHOP transcription rate with a Hill function:

$$A_{6,hill} = \frac{A_6^n}{A_6^n + K_{A2C}^n}\,, \tag{15}$$

where n and K_{A2C} are the exponent and threshold in the Hill-function. Note that because there is not a clear peak in the dynamics of pXBP1(S) or ATF4 shown in Fig. 2D in the main text, a Hill function with an exponent larger than one is not needed to describe the effect of pXBP1(S) and ATF4 on CHOP (i.e., the fitting performance is not improved). Hence, for the sake of simplicity, we only used a Hill function for pATF6(N).

In addition to the six state variables, the exposure-related stressor S_i is a dynamic variable whose kinetics do not depend on the other system states. The intra-cellular concentration of the applied compound (S_c) is described explicitly with the following pharmacokinetics (see the supplementary subsection "Describing cellular exposure with a two-compartment model" for details about its derivation):

$$S_c = E_i \left(e^{(-\tau_2 t)} - e^{(-\tau_1 t)}\right) H(t). \tag{16}$$

Here E_i represents the effective intra-cellular concentration of the applied compound, with the subscript i denoting the applied concentration in μM. For 1 μM, we set $E_1 = 1$; for the other four concentrations we assign four free parameters that are estimated (see Table S1). $H()$ stands for the Heaviside function. We consider the stressor to affect the signaling network only when a threshold θ_{th} is crossed. We describe this by the above discussed S_i, i.e., the effective rate at which unfolded proteins are formed due to the stressor:

$$S_i = e_s\,(S_c - \theta_{th}) H(S_c - \theta_{th}), \tag{17}$$

where e_s scales the effective intra-cellular concentration of tunicamycin to unfolded proteins. At equilibrium, the total production rate of unfolded proteins is $\frac{E_t}{1+P_{act}} + s_s$.

For each GFP-reporter cell line, we introduce scaling and offset parameters denoted as e_{GFP} and s_{GFP}, respectively. Those two parameters transform the state in the ODE to the observable. For example, for ATF4 we formulated the observable A_4^o as

$$A_4^o = e_{atf4}\, A_4 + s_{atf4}. \tag{18}$$

Hence, to map the concentrations of the proteins to the GFP intensities, we introduce eight parameters for the four UPR cell lines: e_{xbp1}, s_{xbp1}, e_{atf4}, e_{chop}, s_{xbp1}, s_{atf4}, s_{bip}, and s_{chop}.

All model simulations were conducted in python 2.7.14.

Model calibration and model selection

We fitted our models to the quantified dynamics of reporter cell lines, using the maximum likelihood approach to estimate parameters. Given the nonlinear nature of the model, multiple local optima of parameters could exist in the likelihood landscape. To find the global optimum, we employed a Monte Carlo method with multiple starting values. We generated a set of $N_s = 1000$ starting values $\{\boldsymbol{\theta_s}\}$ in $\boldsymbol{\Theta}$ using Latin hypercube sampling (McKay et al., 2000). We listed the employed boundaries of the parameters in Table S1. For each starting value, we use the Trust-Region-Reflective-Newton method to obtain the local minimum $\boldsymbol{\theta_f}$ (Coleman & Li, 1996). For a

robust and efficient estimation, we incorporate the sensitivity equation (Raue et al., 2013) and a steady state constraint (Rosenblatt et al., 2016) into our local optimization. After applying this local optimization for all starting values, we take the estimate $\hat{\boldsymbol{\theta}} = \boldsymbol{\theta_f}$ with the minimal negative log-likelihood. Numerical optimization relied on the python package scipy. To quantify the uncertainty of parameter estimates, we applied a Hessian-based approach to explore the likelihood around the estimates. We quantified this as a 95% confidence interval of the estimates (Raue et al., 2009) (see details in the Supplement "Covariance matrix of estimates" and confidence intervals of the estimates in Table S1). Moreover, we performed a sensitivity analysis of the impact of single parameters on the CHOP level based on the maximum likelihood estimate, i.e., the most plausible set of parameters based on the measurements (see details in the Supplement "sensitivity analysis").

Plausible models are expected to give a good fit to observations with a relatively small value of the negative-log likelihood at $\hat{\boldsymbol{\theta}}$. We performed a likelihood-ratio-based test to evaluate the goodness of fit to the measurements, as for example applied in (García-Pérez & Alcalá-Quintana, 2015a,b) aiming to get insight into processes underlying temporal-order and simultaneity judgments by observers. Specifically, García-Pérez & Alcalá-Quintana (2015a) focused on a likelihood-ratio based approach to check goodness of fit and García-Pérez & Alcalá-Quintana (2015b) further incorporated the likelihood ratio into a Bayesian test when computing the ratio of two posterior distributions in order to derive a closed-form psychometric function about simultaneity judgments. In general, the test can be used to compare two models by the ratio of their likelihoods, denoted by $\triangle G$, and a p value is computed from a χ^2 distribution. In our case, we used this approach to evaluate whether the data are more compatible with separate incorporation of the ATF6 branch (with estimates $\boldsymbol{\theta_2}$) rather than with lumping ATF6 and XBP1 into a single branch (with estimates $\boldsymbol{\theta_1}$).

Modeling of knockdown conditions

We simulated the calibrated model by incorporating single knockdown perturbations with siRNA treatments. We focused on the knockdowns with siDDIT3 and siATF4, and siATF6, setting the knockdown efficiencies at the values estimated by the analysis of the TempO-seq data. To account for variability of knockdown efficiencies over experiments and over time from different assays, we varied the knockdown efficiency by 20% more or less than the reference value and simulated the model accordingly.

Here we describe how we model knockdown experiments by siRNA treatments. The dynamics of the mRNA can be described by the following differential equation:

$$\tau_m \frac{d}{dt}[\text{mRNA}] = \lambda_m + \text{tf(t)} - d_m\,[\text{mRNA}]\,, \tag{19}$$

where [mRNA] represents the amount of mRNA of interest, τ_m is the time constant of the mRNA, tf(t) is mRNA production rate due to TF activity, λ_m denotes the basal production rate, and d_m is the degradation rate of the mRNA. We consider knockdown of a gene of interest to increase the mRNA degradation rate compared to the control case. To study how this affects the protein dynamics over time, we first write the equation for the protein:

$$\tau_p \frac{d}{dt}[\text{protein}] = \lambda_p[\text{mRNA}] - d_p\,[\text{protein}]\,, \tag{20}$$

where [protein] represents the amount of protein of interest, τ_p is the time constant of the protein and d_p is the degradation rate of the protein.

Considering transcription to be much faster than (post-)translational processes, i.e. $\tau_m \ll \tau_p$, the mRNA will be at equilibrium, i.e., $[\text{mRNA}](t) = \frac{\lambda_m + \text{tf(t)}}{d_m}$.

Substitution of this relation into the translation step in (20) gives

$$\tau_p \frac{d}{dt}[\text{protein}] = \lambda_p \frac{\lambda_m}{d_m} + \lambda_p \frac{\text{tf(t)}}{d_m} - d_p\,[\text{protein}]. \tag{21}$$

Lumping $\frac{\lambda_m}{d_m}$ into λ_p^* and $\lambda_p \frac{\lambda_m}{d_m}$ into μ_p^* results in:

$$\tau_p \frac{d}{dt}[\text{protein}] = \mu_p^* + \lambda_p^* \text{tf} - d_p\,[\text{protein}]. \tag{22}$$

In this equation, μ_p^* and λ_p^* incorporate the effects of the increased mRNA degradation upon knockdown. Thus, these parameters are expected to decrease when cells are pre-treated with siRNA knockdowns. We define the knockdown efficiency e_{KD} as $1 - \frac{[mRNA]_{KD}}{[mRNA]}$, which equals $1 - \frac{d_m}{d_{m,KD}}$, where $d_{m,KD}$ is the mRNA degradation rate upon knockdown. Then we obtain $d_{m,KD} = \frac{d_m}{1-e_{KD}}$, which propagates into the parameters for protein formation as $\mu_{p,KD}^* = (1 - e_{KD})\,\mu_p^*$ and $\lambda_{p,KD}^* = (1 - e_{KD})\,\lambda_p^*$. In conclusion, the knockdowns can be simulated by decreasing the protein production rates with a multiplier based on the measured knockdown efficiency.

For ATF4, ATF6 and CHOP, for which we obtained knockdown efficiencies, we thus perturbed the production rates as follows: For siATF4, we set $\beta_2 = (1 - e_{KD})\hat{\beta_2}$ and $b_0 = (1 - e_{KD})\hat{b_0}$, where $\hat{\beta_2}$ and $\hat{b_0}$ are the estimated values in the absence of knockdown. For siATF6, we set $\beta_3 = (1 - e_{KD})\hat{\beta_3}$, where $\hat{\beta_3}$ is the estimated value in the absence of knockdown. For siDDIT3, we set $\gamma_2 = (1 - e_{KD})\hat{\gamma_2}$, $\alpha_3 = (1 - e_{KD})\hat{\alpha_3}$, $\alpha_4 = (1 - e_{KD})\hat{\alpha_4}$, and $\alpha_6 = (1 - e_{KD})\hat{\alpha_6}$, where $\hat{\gamma_2}$, $\hat{\alpha_3}$, $\hat{\alpha_4}$, and $\hat{\alpha_6}$ are the estimated values in the absence of knockdown.

Supplementary Details

Analysis of single-cell data

For the analysis of single-cell imaging data, we applied the following steps: First, for each of three biological replicates (each consisting of two pooled technical replicates), we calculated the geometric mean (denoted by I) based on GFP measurements for thousands of cells per image well at all time points and for all treatment conditions. Second, from this analysis we obtained the minimum (denoted by I_{min}) and maximum (denoted by I_{max}) of these geometric means with respect to all conditions and time points (separately for every cell line in every plate). We then applied min-max normalization to obtain the normalized intensity (denoted by I_N) each time point according to:

$$I_N = \frac{I - I_{min}}{I_{max} - I_{min}}\,. \tag{23}$$

Third, we interpolated the normalized means to the time points from 1h to 22h as described in the main text (note that some treatment conditions only had data before 23h). Finally, we took the arithmetic mean and standard deviation of the interpolated data for the biological replicates, which we used for further model fitting purposes.

Describing cellular exposure with a two-compartment model

To describe the exposure of cells to the chemical tunicamycin, we introduce a two-compartment model describing the concentrations of the chemical in the medium ($[C_1]$) and in the cells ($[C_2]$):

$$\begin{cases} \frac{d[C_1]}{dt} &= [D]\delta(t) - \tau_1[C_1]\,, \\ \frac{d[C_2]}{dt} &= \tau_1[C_1] - \tau_2[C_2]\,. \end{cases} \tag{24}$$

Here, τ_1 is the cellular absorption rate from the medium, τ_2 is the degradation rate of the chemical within cells and $[D]$ and $\delta(t)$ are the applied exposure and unit pulse input functions, respectively. To obtain the solution of the above set of ODEs, one can take a convolution: In general, for $g(t) = \int f(\tau)\, h(t-\tau)d\tau$, $g(t)$ is the output function, $f(t)$ is the input function and $h(t)$ is the transfer function of the linear system, which can be derived by Laplace transformation. In our case, the transfer functions for $[C_1]$ and $[C_2]$ are $\exp(-\tau_1 t)H(t)$ and $\exp(-\tau_2 t)H(t)$, respectively. For $[C_1](t)$ we then obtain the solution $[C_1](t) = [D]\exp(-\tau_1 t)H(t)$. Furthermore, for $[C_2](t)$ we obtain:

$$[C_2](t) = [D]\exp(-\tau_2 t)\left(\exp(-(\tau_2-\tau_1)t)(\tau_2-\tau_1)^{-1} - (\tau_2-\tau_1)^{-1}\right). \tag{25}$$

This simplifies to:

$$[C_2](t) = (\tau_2-\tau_1)^{-1}\tau_1[D](\exp(-\tau_1 t) - \exp(-\tau_2 t)). \tag{26}$$

To avoid structural non-identifiability issues, we absorb the term $\tau_1(\tau_2-\tau_1)^{-1}$ into the parameter e_s that scales the stressor (see Eq. (17) in main text), leaving us with:

$$[C_2](t) = [D](\exp(-\tau_1 t) - \exp(-\tau_2 t))H(t). \tag{27}$$

Activation of the three UPR sensors

Our calibrated model can be used to provide insight into the activation speed of the three UPR branches. We therefore quantified the moment at which the active forms of the sensors (active IRE1α, active PERK, and free ATF6) reach their half-maximal value, taking 1 μM of tunicamycin as a representative case (Fig. S5).

Effect of Hill coefficient on CHOP transcription

Because the estimated value of the Hill coefficient in the relation between $A_{6,hill}$ and A_6 (Eq. (15) in main text) is very high ($n = 46.32$), this implies a switch-like response of CHOP transcription with increasing pATF6(N), questioning the suitability of a lower n value. In the model, the sigmoid dependency of CHOP expression on pATF6(N) levels is complemented by linear dependencies on XBP1 (with parameter α_3) and on ATF4 (with parameter α_4) (Eq. (14) in main text). In order to understand the effect of the Hill exponent n on CHOP regulation, we varied n over a wide range (from 0 to 200) while keeping the other model parameters the same and plotted the predicted CHOP response in a two-dimensional heat-map with time on the horizontal axis and n on the vertical axis (Fig. S6). This analysis shows that an increase of the exponent beyond the calibrated value ($n = 46.32$) still has a clearly noticeable effect on the dynamics of CHOP. Consistent with sensitivity of the CHOP response to n, high values of n lead to a more pronounced peak in CHOP levels and an even more step-like response of CHOP transcription with pATF6(N) concentration and with time compared to low values of n (Figs. S7 and S8). As a side note, because CHOP in our model does not provide feedback to any of the other state variables, the Hill coefficient n will not affect the pATF6(N) concentration itself. Thus, this analysis shows that the value of the Hill exponent is important in determining the CHOP dynamics, especially around the time of its peak.

Contribution of pXBP1(S) and ATF4 to CHOP production

According to the model calibration, the coefficients describing pXBP1(S)-mediated and ATF4-mediated CHOP transcription respectively are $\alpha_3 = 31.77$ (pXBP1(S)), and $\alpha_4 = 27.64$ (ATF4), suggesting approximately equal contribution of these two TFs. However, besides these coefficients, the concentrations of ATF4 and pXBP1(S) themselves also have an important role in the contribution of the TFs to CHOP transcription. Because the amount of pXBP1(S) is much lower than ATF4 (Fig. S9), this concentration effect dominates when one considers the product terms $\alpha_3 X$, $\alpha_4 A$ and $\alpha_6 A_{6,h}$ and the pXBP1(s) contribution to CHOP transcription is small (Fig. 4B-D).

Choice of parameter ranges

During model calibration, we did not restrict the allowed parameter ranges taking full biophysical details into consideration because the units of the normalized intensities in our imaging data were arbitrary, precluding determination of the unit of concentrations. Rather, we required all parameters (besides s_s) to be positive and based our choices of parameter ranges on trial simulations with Trusina et al.'s previously published model parameterization (Trusina et al., 2008). The parameter ranges considered and the units of parameters are provided in Table S1. Note that the high values for some of the Michaelis-Menten constants are due to the high levels of unfolded proteins in our simulations (for which we have no measurements) and should be interpreted in a relative rather than absolute manner.

Covariance matrix of estimates

In order to study the uncertainty of the estimated parameter values, we utilize the Jacobian matrix ($\mathbf{J}$) to approximate the Hessian matrix $\mathbf{H}$:

$$\mathbf{H} = \mathbf{J}^T \mathbf{J}\, S(\theta)\,. \tag{28}$$

Here, the mean squared error $S(\theta)$ (i.e., the residual sum of squares divided by the number of degrees of freedom) is given by

$$S(\theta) = \frac{\mathbf{R}^T \mathbf{R}}{n_D - n_\theta}\,, \tag{29}$$

where R is the vector containing the residuals between model prediction and data, $n_D = 440$ denotes the number of data points and $n_\theta = 47$ denotes the number of free parameters in our

model with ATF6 branch. The squares of the standard errors of the estimates are the diagonal items in the co-variance matrix, expressed as the inverse matrix $\mathbf{H}^{-1}$. The standard errors of all parameters are presented in Fig. S3. We multiplied these values by 1.98 to obtain confidence intervals (CIs) (Raue et al., 2009) (shown together with the estimates in Table S1). Note that although the amount of experimental measurements is large compared to the number of parameters in our case, the CI for some parameters may be underestimated by the Hessian-based estimate.

Sensitivity analysis

We performed a sensitivity analysis to quantify the importance of the model parameters around our maximum likelihood estimate. Because CHOP is an important determinant in downstream cell fate and most of the signalling parameters are expected to indirectly affect the activity of CHOP especially around the peak, we focus on CHOP activity at 16 hours after treatment with 6μM of tunicamycin. Thus, we performed a local sensitivity analysis around the maximal likelihood estimate $\hat{\theta}$ for the model with ATF6.

In the sensitivity analysis, we omitted parameters that should have no impact on CHOP in conditions of 6μM tunicamycin treatment. Specifically, these are the effective tunicamycin concentrations of 2, 4, 12 μM, i.e. E_2, E_4 and E_{12}. Moreover, we omitted the three pairs of the scaling coefficients (e_{XBP1}, e_{ATF4}, and e_{BIP}) and offsets (s_{XBP1}, s_{ATF4}, and s_{BIP}) for the non-CHOP reporter cell lines. We varied each of the remaining parameters by both increasing and decreasing them by a small value (δ_θ) from its optimum. Subsequently, we quantified the sensitivity using the following equation:

$$\frac{\Delta C}{\Delta \theta_i} = \frac{C(\theta + \delta_\theta) - C(\theta - \delta_\theta)}{2\,\delta_\theta}\,, \tag{30}$$

where for different parameters, we used different δ_θ. For τ_2 and r_U, we chose a value just above the machine precision (3e-16); for other parameters, we set δ_θ to 1e-6$\times\hat{\theta}$, i.e., based on the maximum likelihood estimate. As the sensitivity can be negative or positive and the absolute value of sensitivities has a broad range, we plotted the log10 of the absolute values of the calculated sensitivities, with the colour indicating positive or negative sensitivity (Fig. S4). The most straightforward parameters having a positive impact on CHOP are the scaling parameters e_C and s_C, and parameters representing direct inputs like E_6 and e_s. As expected, parameters with a negative impact typically arise from those promoting degradation of CHOP, like r_C.

Supplemental References

Coleman, T. F., & Li, Y. (1996). An interior trust region approach for nonlinear minimization subject to bounds. *SIAM Journal on optimization*, *6*(2), 418–445.

Di, Z., Herpers, B., Fredriksson, L., Yan, K., van de Water, B., Verbeek, F. J., & Meerman, J. H. (2012). Automated analysis of nf-κb nuclear translocation kinetics in high-throughput screening. *PloS one*, *7*(12), e52337.

Diedrichs, D. R., Gomez, J. A., Huang, C.-S., Rutkowski, D. T., & Curtu, R. (2018). A data-entrained computational model for testing the regulatory logic of the vertebrate unfolded protein response. *Molecular biology of the cell*, mbc–E17.

Dowle, M., Srinivasan, A., Gorecki, J., Chirico, M., Stetsenko, P., Short, T., ... others (2018). Package 'data. table'.

Garcia-Alonso, L., Ibrahim, M. M., Turei, D., & Saez-Rodriguez, J. (2018). Benchmark and integration of resources for the estimation of human transcription factor activities. *bioRxiv*, 337915. doi: 10.1101/337915

García-Pérez, M. A., & Alcalá-Quintana, R. (2015a). Converging evidence that common timing processes underlie temporal-order and simultaneity judgments: A model-based analysis. *Attention, Perception, & Psychophysics*, *77*(5), 1750–1766.

García-Pérez, M. A., & Alcalá-Quintana, R. (2015b). Visual and auditory components in the perception of asynchronous audiovisual speech. *i-Perception*, *6*(6), 2041669515615735.

Hendriks, G., Atallah, M., Morolli, B., Calléja, F., Ras-Verloop, N., Huijskens, I., ... Vrieling, H. (2011). The toxtracker assay: novel gfp reporter systems that provide mechanistic insight into the genotoxic properties of chemicals. *Toxicological Sciences*, *125*(1), 285–298.

Hiemstra, S., Niemeijer, M., Koedoot, E., Wink, S., Klip, J. E., Vlasveld, M., ... Water, B. v. d. (2016). Comprehensive landscape of nrf2 and p53 pathway activation dynamics by oxidative stress and dna damage. *Chemical research in toxicology*, *30*(4), 923–933.

Love, M. I., Huber, W., & Anders, S. (2014). Moderated estimation of fold change and dispersion for rna-seq data with deseq2. *Genome biology*, *15*(12), 550.

Mav, D., Shah, R. R., Howard, B. E., Auerbach, S. S., Bushel, P. R., Collins, J. B., ... others (2018). A hybrid gene selection approach to create the s1500+ targeted gene sets for use in high-throughput transcriptomics. *PloS one*, *13*(2), e0191105.

McKay, M. D., Beckman, R. J., & Conover, W. J. (2000). A comparison of three methods for selecting values of input variables in the analysis of output from a computer code. *Technometrics*, *42*(1), 55–61.

Neuwirth, E. (2014). Rcolorbrewer: Colorbrewer palettes, r package version 1.1-2 http://cran. *R-project. org/package= RColorBrewer*.

Niemeijer, M., Hiemstra, S., Wink, S., den Hollander, W., ter Braak, B., & van de Water, B. (2018). Systems microscopy approaches in unraveling and predicting drug-induced liver injury (dili). In *Drug-induced liver toxicity* (pp. 611–625). Springer.

Poser, I., Sarov, M., Hutchins, J. R., Hériché, J.-K., Toyoda, Y., Pozniakovsky, A., ... others (2008). Bac transgeneomics: a high-throughput method for exploration of protein function in mammals. *Nature methods*, *5*(5), 409.

Raue, A., Kreutz, C., Maiwald, T., Bachmann, J., Schilling, M., Klingmüller, U., & Timmer, J. (2009). Structural and practical identifiability analysis of partially observed dynamical models by exploiting the profile likelihood. *Bioinformatics*, *25*(15), 1923–1929.

Raue, A., Schilling, M., Bachmann, J., Matteson, A., Schelke, M., Kaschek, D., ... others (2013). Lessons learned from quantitative dynamical modeling in systems biology. *PloS one*, *8*(9), e74335.

Rosenblatt, M., Timmer, J., & Kaschek, D. (2016). Customized steady-state constraints for parameter estimation in non-linear ordinary differential equation models. *Frontiers in cell and developmental biology*, *4*, 41.

Trusina, A., Papa, F. R., & Tang, C. (2008). Rationalizing translation attenuation in the network architecture of the unfolded protein response. *Proceedings of the National Academy of Sciences*, *105*(51), 20280–20285.

Wickham, H. (2010). ggplot2: elegant graphics for data analysis. *J Stat Softw*, *35*(1), 65–88.

Wickham, H. (2017). tidyr: Easily tidy data with'spread ()'and'gather ()'functions, 2017. *URL https://CRAN. R-project. org/package= tidyr. R package version 0.6*, *1*, 248.

Wickham, H., et al. (2011). The split-apply-combine strategy for data analysis. *Journal of Statistical Software*, *40*(1), 1–29.

Wink, S., Hiemstra, S., Herpers, B., & van de Water, B. (2017). High-content imaging-based bac-gfp toxicity pathway reporters to assess chemical adversity liabilities. *Archives of toxicology*, *91*(3), 1367–1383.

Wink, S., Hiemstra, S., Huppelschoten, S., Danen, E., Niemeijer, M., Hendriks, G., ... van de Water, B. (2014). Quantitative high content imaging of cellular adaptive stress response pathways in toxicity for chemical safety assessment. *Chemical research in toxicology*, *27*(3), 338–355.

Ye, J., Rawson, R. B., Komuro, R., Chen, X., Davé, U. P., Prywes, R., ... Goldstein, J. L. (2000). Er stress induces cleavage of membrane-bound ATF6 by the same proteases that process srebps. *Molecular cell*, *6*(6), 1355–1364.

Yeakley, J. M., Shepard, P. J., Goyena, D. E., VanSteenhouse, H. C., McComb, J. D., & Seligmann, B. E. (2017). A trichostatin a expression signature identified by tempo-seq targeted whole transcriptome profiling. *PLoS One*, *12*(5), e0178302.

Zhang, Z. (2016). Reshaping and aggregating data: an introduction to reshape package. *Annals of translational medicine*, *4*(4).